International Journal of Mechanical Sciences 289 (2025) 109976

Contents lists available at ScienceDirect

International Journal of Mechanical Sciences

journal homepage: www.elsevier.com/locate/ijmecsci

Morphing surfaces inspired by thick-panel origami

Chenying Liu [a,b,*], Fufu Yang [c], Perla Maiolino [a,b,d], Zhong You [a,*]

[a] Department of Engineering Science, University of Oxford, Parks Road, Oxford, OX1 3PJ, Oxfordshire, United Kingdom
[b] Oxford Robotics Institute, University of Oxford, 23 Banbury Road, Oxford, OX2 6NN, Oxfordshire, United Kingdom
[c] School of Mechanical Engineering and Automation, Fuzhou University, Xueyuan Road, Fuzhou, 350116, Fujian, China
[d] Department of Mechanical, Energy, Management and Transport Engineering DIME, University of Genoa, Via All'Opera Pia, Genoa, 15, 16145, Liguria, Italy

ARTICLE INFO

Keywords:
Thick-panel origami
Uniform thickness
Programmable shape-changing
Spatial overconstrained linkage
Kinematic mapping and analysis
Origami tessellation

ABSTRACT

Origami, derived from the Japanese words 'ori' meaning fold and 'kami (gami)' meaning paper, has found extensive engineering applications in modern days. In the last decade, an emerging venue lies in robotics, where origami is taken as an exoskeleton of a robot to generate desired behaviours. The motions of origami are often coupled through in-built folds, leading to lower or more controllable degrees of freedom (DoFs) while still exhibiting shape-changing properties akin to those of soft materials. This unique feature enhances the compliance of robots without compromising their controllability. The prevalent use of zero-thickness sheets makes origami robots prone to fatigue, necessitating the incorporation of origami made from durable thick materials. Whilst substantial attempts have been made in the field of thick-panel origami, the concept was originally conceived for space solar panels. Hence, existing research predominantly focuses on properties such as flat foldability and kinematic equivalence. Consequently, many designs also end up with rigid panels of non-uniform thicknesses, complicating the fabrication process. As a result, roboticists, who are interested in shape-changing origami as well as its fabrication and control simplicity, often find it challenging to directly implement those thick panels in the robotic design. This work addresses these research gaps by introducing the first systematic approach to designing uniform-thickness origami capable of shape-changing, referred to as morphing surfaces. Such surfaces are enabled by a comprehensive mapping between thick-panel origami and spatial overconstrained linkages, followed by various tessellation methods. Bending, expanding, twisting, and complex motion behaviours will be realised on the proposed surfaces, all with a single DoF. The surfaces are thus readily applicable in robotics for targeted functions.

1. Introduction

Origami has found diverse applications across scales, ranging from the microworld with examples likes DNA origami [1] and heart stent [2] to macroscale domains including deployable shelters [3] and foldable antennas [4]. The in-built crease structure of origami offers the potential to emulate soft-bodied properties, positioning it as a viable alternative to robots constructed solely from soft materials [5]. Once folded, two-dimensional (2D) paper sheets can be transformed into intricate three-dimensional (3D) configurations, which demonstrate behaviours such as bending [6], expanding [7], or twisting [8]. They form the fundamental motions for robots to execute their functionalities.

The integration of origami into robotic structures has yielded advantages over both soft-material robots and those based on rigid links and joints. Using origami as a skeleton not only simplifies the design process but also facilitates the prediction and control of robot motions. Successful examples include but are not limited to origami robots that are capable of grasping [9], manipulation [8], and locomotion [10].

Nonetheless, it is crucial to highlight that limitations still exist in the current design of origami robots. First of all, up to the present, the majority of, if not all, origami robots are constructed from existing patterns based on zero-thickness sheets [11]. As such, paper [12] and polymer films [13] are the primary materials used in origami robots, which are susceptible to fatigue from repeated folding and unfolding. 3D-printed layers [14] are also exploited, which overlook the material thickness and cause inaccuracies in motion predictions. Moreover, to be functional, many patterns need to be pre-folded into cylindrical forms from 2D sheets or directly made into 3D configurations, complicating the manufacturing process. Lastly, despite the abundance of origami patterns, there is still a lack of flexibility when designing desired motions. For example, the twisting behaviour of Kresling origami is intrinsically coupled with axial extension and contraction [15], restricting the range of motion possibilities. New designs of origami are necessitated.

---

* Corresponding authors.
E-mail addresses: chenying.liu@eng.ox.ac.uk, chenying.liu@chch.ox.ac.uk (C. Liu), zhong.you@eng.ox.ac.uk (Z. You).

https://doi.org/10.1016/j.ijmecsci.2025.109976
Received 30 May 2024; Received in revised form 13 September 2024; Accepted 12 January 2025

A few years ago, a novel approach was introduced to design origami with finite and non-negligible thickness, wherein creases are replaced by folding lines (folds) at either the top or bottom surfaces of a rigid thick panel [16]. The new mechanical model is known as thick-panel origami (TPO). With the advent of this concept, it has become feasible to consider material thickness in the design of origami, opening avenues for new patterns and the incorporation of durable materials.

Various endeavours have been undertaken in the realm of TPO. A common approach is to seek inspiration from existing zero-thickness patterns and adjust the panel thickness, thereby establishing a mapping with spatial linkages. Commonly investigated patterns include Miura-ori origami [17], Diamond or Yoshimura origami [18,19], Waterbomb origami [20], and Ron Resch origami [21], all of which are modelled as an assembly of spatial overconstrained linkages covering the Bennett linkage [22] and the plane-symmetric Bricard linkage [23]. Researchers also draw inspiration from kirigami, a derivation and less restrictive form of origami, by adding slits or cuts in the patterns to create thick-panel origami. The approach results in a more extensive mapping with spatial linkages, such as the 6R Waldron hybrid linkage [24] and various 8R linkages [25–27].

Given the distinct kinematic model of TPO in comparison to its zero-thickness counterpart, the majority of, if not all, thick ones have reduced DoFs, offering additional potential for simplified control in robotics. Moreover, some possess bifurcations, allowing the origami to transit into different configurations at a specific state without an increase in its overall mobility. Such phenomena make a natural link to the concept of reconfiguration, where robots can change their morphology to better adapt to the environment. So far, however, TPO remains exclusive to the robotics community, regardless of substantial advancements in its design and analysis. This inaccessibility is attributed to several barriers as listed below.

Firstly, roboticists aspire to harness the shape-changing capabilities of origami, yet the motion possibilities of thick-panel variations remain constrained. Currently, TPO is derived from a limited set of spatial linkages, leaving uncertainty about the applicability of other spatial linkages.

Secondly, the prevalent focus of engineers on TPO design is its flat foldability, i.e., whether the origami can be folded into a compact volume. This is rooted in TPO's initial purpose for space solar panels. With this in mind, all TPO designs, except for the thick-panel Diamond origami and the ones using slits, end up with non-uniform thicknesses - a characteristic not suitable for fabrication simplicity.

Lastly, while kirigami offers the potential for uniform thickness, the incorporation of slits often follows a trial-and-error approach, not to mention that some kirigami designs are just a simple geometric extension of the origami version without cuts.

In response to the aforementioned gaps and limitations, this research will introduce a more explicit, systematic, and comprehensive design methodology focusing on origami with uniform-thickness panels. The goal is to create a library of shape-changing units. Each consists of interlinked rigid panels with uniform thickness and has a single mobility. This unit library is designed to be accessible to anyone interested in morphable structures, offering the flexibility to select units and combine them to suit complex shape-changing behaviours. In particular, with appropriate tessellations or assemblies, we have combined some of the units together to form morphing surfaces capable of various motions, such as bending, expanding, or twisting — illustrated with examples in this paper. The results strive to expedite the design theory of TPO and make it more suitable for targeted robotic applications.

2. Morphing units

A systematic approach is proposed to design modular shape-changing structures with uniform thickness, namely morphing units. Inspired by TPO and the abundance of 6R spatial overconstrained linkages [28], each unit is a closed chain of rigid panels connected by top or bottom folds. A library of mobile units is derived, whose kinematic behaviours are detailed.

2.1. Design methodology

2.1.1. 2D patterns and geometric features

In origami, a base is the simplest element whose tessellation forms the entire origami pattern. Fig. 1 shows four origami bases which will be used to construct morphing units, including a single-vertex pattern (SVP), a single-slit pattern (SSP), a triangular-void pattern (TVP), and a quadrilateral-void pattern (QVP). We acknowledge that the four particular bases cannot cover all possible patterns but the reason for selecting them is detailed in Appendix A.

If we replace the sheet forming the base with panels of uniform thickness h, a unit is obtained. Each unit is composed of six rigid panels which are joined by folds at either the top or bottom of panels as shown in Fig. 1(e). These folds are numbered clockwise from 1 to 6 and P_i refers to the panel between folds i and $i+1$, where $i+1$ returns to 1 when $i=6$. The panels are connected to form a single closed loop. When no connection exists between two adjacent panels such as P_2 and P_5 in the SSP, a slit is introduced. Multiple slits result in a void in the origami base, which yields the TVP and QVP.

For each base, the panels and their connecting folds are essentially a 6R closed chain if it can be folded. According to the Kutzbach criterion, its DoF is zero. To be mobile, the linkage must be overconstrained. We exclude the cases where:

- all folds are on the same surface of a unit, making it a spherical linkage or its assembly; or
- only hinge-like motion exists due to aligned folds on the same surface.

Denavit-Hartenberg (DH) parameters, as detailed in Appendix B, are used to model each unit, where fold i is a joint associated with coordinate z_i and revolute variable θ_i. Physically, the variable θ_i can be converted into the dihedral angle ω_i, namely the angle between the side walls of two connected panels, which is also illustrated in Fig. 1(e). Since the two panels cannot penetrate each other, ω_i must satisfy

$$0 \le \omega_i \le 180^\circ,\ i=1,2,\dots,6 \tag{1}$$

where each angle is continuous, starting from zero when the unit is fully unfolded. When one dihedral angle reaches its limit first, other angles cannot move forward, if the linkage has only one DoF.

For a mobile unit, its geometric conditions are characterised by its 2D base shape and fold arrangement. To understand the underlying mathematics, panel P_i is defined by a sector angle $\alpha_{\mathrm{P}i}$, which is the angle between its two adjacent folds as shown in Fig. 1(a). If a base has a slit or void, the sector angle is decided by two side angles of the panel, $\alpha_{\mathrm{P}ii}$ and $\alpha_{\mathrm{P}i(i+1)}$. For instance, the SSP in Fig. 1(b) gives $\alpha_{\mathrm{P}2}=\alpha_{\mathrm{P}22}+\alpha_{\mathrm{P}23}-180^\circ$.

Mathematically, all sector angles must satisfy

$$\sum_{i=1}^{6} \alpha_{\mathrm{P}i} = 360^\circ \tag{2}$$

where the associated angles are further restricted by constraints in Table 1.

In addition, the TVP and QVP have an additional constraint coming from the void, i.e., the side lengths of each void must be positive and compatible with its interior angles.

By observation, the four bases and their derived units exhibit a few kinematic features as follows. With the aforementioned geometric constraints, these features are subsequently used to evaluate whether a unit is mobile.

- When certain geometric conditions are satisfied, the four bases are kinematically equivalent and repeated cases are thus not discussed. For example,
  - the SVP is a special case of the SSP when the slit length d reduces to zero;

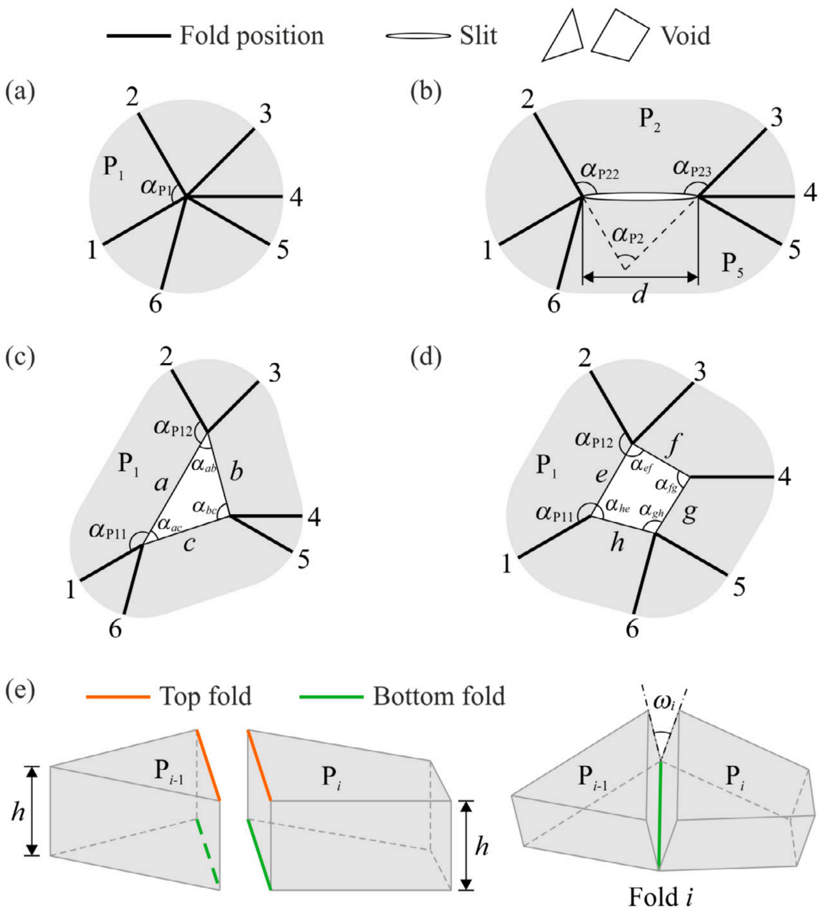

Fig. 1. Origami bases. **(a)** Single-vertex pattern where all folds intersect at a single point. **(b)** Single-slit pattern where the folds create two intersecting points. Note that the gap in the slit is for illustration only and should be infinitely small. **(c)** Triangular-void pattern with three intersecting points. **(d)** Quadrilateral-void pattern. **(e)** Possible fold locations at the top or bottom of adjacent panels and the associated dihedral angle.

  - the QVP becomes an SSP when $\alpha_{\mathrm{P}34} = \alpha_{\mathrm{P}61} = 180°$ as shown in Fig. 2(a); and
  - the QVP is equivalent to a TVP when the intersecting points between folds 1 and 6, folds 4 and 5, as well as folds 2 and 3, can form a triangle, as shown in Fig. 2(b).

- In most cases, the link length between folds i and $i+1$ is either h or zero. Specifically, when the two folds are both top or bottom folds, they intersect with each other on the same plane, thus producing a link length of 0. If one is the top fold and the other is the bottom fold, the link length becomes h. All possibilities are enumerated in Fig. 3, where equivalent ones are removed.
- The link twist between folds i and $i+1$ is

$$\alpha_{i(i+1)} = \alpha_{\mathrm{P}i} \text{ or } \alpha_{i(i+1)} = 360° - \alpha_{\mathrm{P}i} \tag{3}$$

  which also depends on the arrangement of folds i and $i+1$, assuming that the z direction of each fold points outwards from the centre.
- All folds on the SVP as well as folds 1 and 4 on the SSP have zero joint offsets. To create zero offset for any other fold i, either case below must be satisfied.
  - Folds $i-1$, i, and $i+1$ intersect at the same point on the 2D base. For instance, the TVP in Fig. 4(a) has $\alpha_{\mathrm{P}12} = \alpha_{\mathrm{P}34} = \alpha_{\mathrm{P}56} = 180°$. Folds 1, 2, and 6 meet, yielding $R_1 = 0$, which also applies to R_3 and R_5. Hence, $R_1 = R_3 = R_5 = 0$ holds. Similarly, the QVP in Fig. 4 has $R_2 = R_3 = 0$ when $\alpha_{\mathrm{P}11} = \alpha_{\mathrm{P}34} = 180°$.
  - Fold i is parallel to fold $i+1$. For instance, as shown in Fig. 4(c), $\alpha_{\mathrm{P}22} + \alpha_{\mathrm{P}23} = 180°$, giving zero joint offset for fold 2 or 3. When $\alpha_{\mathrm{P}22} = \alpha_{\mathrm{P}23} = 90°$ as shown in Fig. 4(d), both R_2 and R_3 are zero. Note that in such cases, the link length between folds i and $i+1$ need to be recalculated and the link twist $\alpha_{i(i+1)} = 0$.

Table 1
Geometric constraints of 2D origami bases.

2D base	Geometric constraints
SVP	$0 < \alpha_{\mathrm{P}i} < 360°,\ i = 1, 2, \ldots, 6$
SSP	$\alpha_{\mathrm{P}2} = \alpha_{\mathrm{P}22} + \alpha_{\mathrm{P}23} - 180°,\ \alpha_{\mathrm{P}5} = \alpha_{\mathrm{P}55} + \alpha_{\mathrm{P}56} - 180°$ $\alpha_{\mathrm{P}1} + \alpha_{\mathrm{P}22} + \alpha_{\mathrm{P}56} + \alpha_{\mathrm{P}6} = 360°,\ \alpha_{\mathrm{P}23} + \alpha_{\mathrm{P}3} + \alpha_{\mathrm{P}4} + \alpha_{\mathrm{P}55} = 360°$ $0 < \alpha_{\mathrm{P}i} < 360°,\ i = 1, 3, 4, 6;\ \ 0 < \alpha_{\mathrm{P}ii}, \alpha_{\mathrm{P}i(i+1)} < 360°,\ i = 2, 5$
TVP	$\alpha_{\mathrm{P}i} = \alpha_{\mathrm{P}ii} + \alpha_{\mathrm{P}i(i+1)} - 180°,\ i = 1, 3, 5$ $\alpha_{\mathrm{P}11} + \alpha_{ac} + \alpha_{\mathrm{P}56} + \alpha_{\mathrm{P}6} = 360°,\ \alpha_{\mathrm{P}33} + \alpha_{ab} + \alpha_{\mathrm{P}12} + \alpha_{\mathrm{P}2} = 360°$ $\alpha_{\mathrm{P}55} + \alpha_{bc} + \alpha_{\mathrm{P}34} + \alpha_{\mathrm{P}4} = 360°$ $0 < \alpha_{\mathrm{P}i} < 360°,\ i = 2, 4, 6;\ \ 0 < \alpha_{\mathrm{P}ii}, \alpha_{\mathrm{P}i(i+1)} < 360°,\ i = 1, 3, 5$ $\alpha_{ab} + \alpha_{ac} + \alpha_{bc} = 180°,\ 0 < \alpha_{ab}, \alpha_{ac}, \alpha_{bc} < 180°$
QVP	$\alpha_{\mathrm{P}i} = \alpha_{\mathrm{P}ii} + \alpha_{\mathrm{P}i(i+1)} - 180°,\ i = 1, 3, 4, 6$ $\alpha_{\mathrm{P}12} + \alpha_{\mathrm{P}2} + \alpha_{\mathrm{P}33} + \alpha_{ef} = 360°,\ \alpha_{\mathrm{P}45} + \alpha_{\mathrm{P}5} + \alpha_{\mathrm{P}66} + \alpha_{gh} = 360°$ $\alpha_{\mathrm{P}11} + \alpha_{he} + \alpha_{\mathrm{P}61} = 360°,\ \alpha_{\mathrm{P}34} + \alpha_{fg} + \alpha_{\mathrm{P}44} = 360°$ $0 < \alpha_{\mathrm{P}i} < 360°,\ i = 2, 5;\ \ 0 < \alpha_{\mathrm{P}ii}, \alpha_{\mathrm{P}i(i+1)} < 360°,\ i = 1, 3, 4,$ $\alpha_{ef} + \alpha_{fg} + \alpha_{gh} + \alpha_{he} = 360°, 0 < \alpha_{ef}, \alpha_{fg}, \alpha_{gh}, \alpha_{he} < 180°$

- The quadrilateral void in the QVP can be modified without changing the joint offsets of its equivalent linkage. The only thing that matters with regard to its kinematics is where adjacent folds meet on the 2D base.

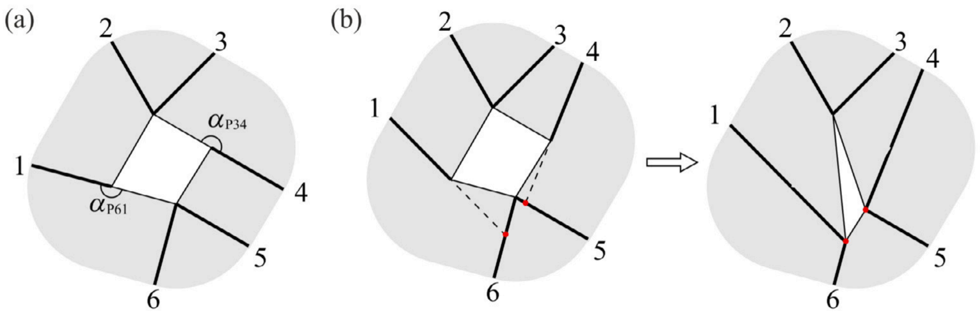

Fig. 2. Special cases of the QVP. **(a)** The QVP is equivalent to the SSP. Folds 1, 5, and 6 intersect with the rest meeting at another point, hence producing the same geometric feature as the SSP in Fig. 1(b). **(b)** The QVP is equivalent to the TVP.

2.1.2. Evaluation process and selection criteria

To explore the possibility of single-DoF morphing units, each pattern in Fig. 3 is examined to see if it meets the requirement of a 6R spatial overconstrained linkage, a full list of which is summarised in Appendix C. The geometric features listed in 2.1.1 are used to simplify the evaluation. The selection criteria for morphing units are as follows.

- A unit must be able to move with all folds. Units with hinge motion only caused by collinear folds are excluded.
- A morphing unit may satisfy the geometric conditions of more than one 6R linkage. It is only counted once if this situation happens.
- Whilst a reference linkage is overconstrained, the unit could have more than one DoF under certain conditions. Such cases are listed in Appendix D.1.
- For some mobile units, physical interference between two disconnected but adjacent panels, such as P_2 and P_5 on the SSP in Fig. 1(b), may occur but it can be eliminated the removal of some of the panels. Such cases are not the focus of this study but will also be summarised in Appendix D.2.
- Bifurcations that cause instantaneous mobility increase are not considered as multiple DoFs.
- Bifurcations of a reference linkage do not mean that they also exist on the unit. Some motion paths of a linkage may not satisfy the geometric constraints in 2.1.1. For instance, they might be physically blocked.

The entire evaluation process is tedious as there are 48 patterns in Fig. 3 and 17 linkages from Appendix C. Instead of providing mathematical derivations for all cases, only a few linkages and patterns are presented. All mobile units are categorised in Section 2.2. Examples of immobile cases are demonstrated in Appendix E.

2.2. Results

After evaluation, the mobile units are categorised into four types based on their reference linkages. This section details their design bases and kinematic behaviours.

2.2.1. Units based on the plane-symmetric Bricard linkage: type 1

As shown in Fig. 5, Units a_1, a_2, and a_3 are based on the plane-symmetric Bricard linkage. Two bottom folds are aligned, giving $\gamma = \alpha + \beta - 180°$. The top folds of Unit a_3 are also collinear with respective sides of the void. Each pattern is symmetric about its bottom folds. The geometric conditions under DH notations defined in Table B.5 are given as follows.

$$\begin{gathered}
a_{12} = a_{34} = a_{45} = a_{61} = h,\ a_{23} = a_{56} = 0 \\
\alpha_{12} = 360° - \alpha_{61} = -\alpha \\
\alpha_{23} = 360° - \alpha_{56} = 180° - \alpha - \beta \\
\alpha_{34} = 360° - \alpha_{45} = \beta \\
R_1 = R_4 = 0,\ R_2 = -R_6 = -\frac{\sin\beta}{\sin(\alpha+\beta)}d,\ R_3 = -R_5 = \frac{\sin\alpha}{\sin(\alpha+\beta)}d
\end{gathered} \tag{4}$$

where d is the equivalent slit length. $d = 0$ for Unit a_1 while d is a positive number for Unit a_2. For Unit a_3, d becomes a negative number and equals $-d_0$, where d_0 is the horizontal width of the void as shown in Fig. 5.

The geometric conditions are then substituted into the closure equation in Appendix B to analyse the kinematic behaviours of each unit. To better understand the physical representation of these units, revolute variables of each fold θ_i are converted to dihedral angles according to Table 2 and the same process applies to all morphing units to be discussed in this study. As such, the closure equations of Units a_1 - a_3 as a general plane-symmetric Bricard linkage are

$$\begin{gathered}
\omega_1 = \omega_4,\ \omega_2 = \omega_6,\ \omega_3 = \omega_5 \\
\tan\frac{\omega_2}{2} = \frac{1}{\cos\alpha}\tan\frac{\omega_1}{2},\ \tan\frac{\omega_3}{2} = \frac{1}{\cos\beta}\tan\frac{\omega_1}{2}
\end{gathered} \tag{5}$$

which is defined as path 1 of these units.

The panel thickness h and equivalent slit length d do not influence the closure equations of Units a_1 - a_3. Taking $\alpha = 60°$ and $\beta = 45°$, path 1 is plotted in Fig. 6 along with simulated models in SOLIDWORKS.

Feng et al. [29] has proven two general motion paths of the plane-symmetric Bricard linkage. It should be noted that only one exists here and the other is blocked. Regardless, it is still worth exploring whether these units have kinematic bifurcations that could lead to other configurations. Instead of solving the closure equations with the possibility of missing a few solutions, the strategy is to evaluate whether the derived 6R linkage of each unit can meet one of the following requirements.

- The 6R spatial linkage can degenerate planar linkages with parallel folds. The simplest case could be two aligned folds.
- The 6R spatial linkage can degenerate 4R/5R spherical linkages, where at least four folds intersect at the same point.
- The 6R spatial linkage can degenerate 4R/5R spatial linkages, i.e., the Bennett linkage, the Myard linkage, and the Goldberg 5R linkage.

Likewise, the same strategy will be applied for all morphing units to be discussed in this section, thus identifying all of their bifurcations.

By observation, Units a_1 - a_3 have aligned bottom folds, producing path 2 as

$$\omega_1 = \omega_4,\ \omega_2 = \omega_3 = \omega_5 = \omega_6 = 0 \tag{6}$$

which is a hinge-like motion. The bifurcation point exists at the unfolded flat state of each unit, i.e., the origin in Fig. 6.

It is also found that Unit a_2 can bifurcate into a 4R spherical linkage as its path 3 when folds 2, 3, 5, and 6 intersect at the same point and the dihedral angles of folds 1 and 4 are hence locked. The geometric conditions for such a situation are

$$\tan\frac{\omega_1}{2} = \tan\frac{\omega_4}{2} = \frac{d\sin\alpha\sin\beta}{h\sin(\alpha+\beta)} \tag{7}$$

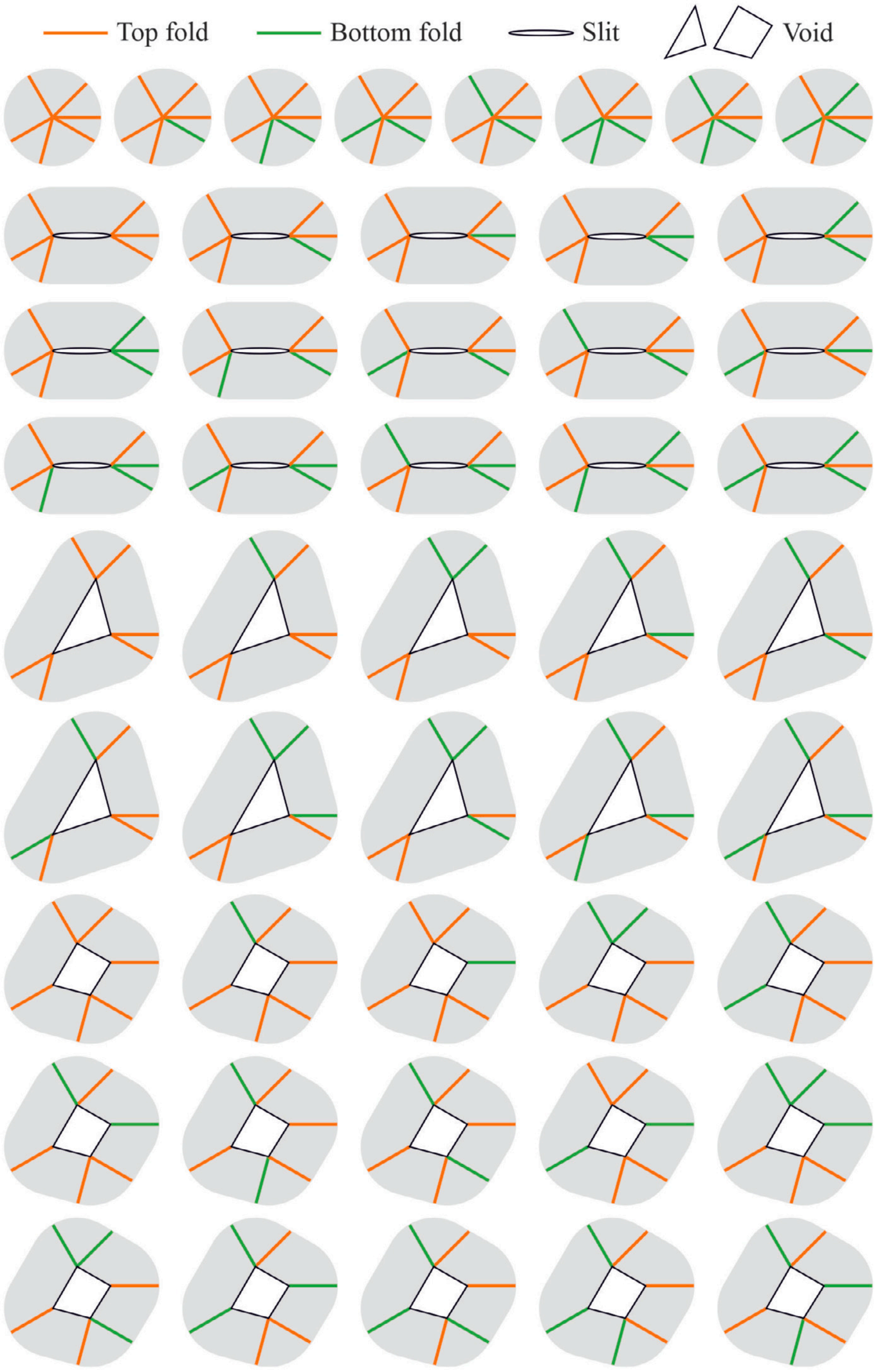

Fig. 3. All possible fold arrangements on the origami bases.

Table 2
Relationship between the revolute variable θ_i and dihedral angle ω_i of morphing units.

θ_i	Unit a_1 - a_3	Unit b_1 - b_3, m_1	Unit c_1 - c_3	Unit m_2
θ_1	$180^\circ + \omega_1$	$180^\circ + \omega_1$	$180^\circ + \omega_1$	$180^\circ + \omega_1 + \arctan \dfrac{a \sin \delta_1}{h}$
θ_2	$180^\circ - \omega_2$	$180^\circ - \omega_2$	$180^\circ - \omega_2$	$180^\circ - \omega_2 - \arctan \dfrac{a \sin \delta_1}{h}$
θ_3	$-\omega_3$	$180^\circ + \omega_3$	$-\omega_3$	$-\omega_3 - \arctan \dfrac{b \sin \delta_2}{h}$
θ_4	$180^\circ + \omega_4$	$180^\circ - \omega_4$	$180^\circ + \omega_4$	$180^\circ + \omega_4 + \arctan \dfrac{b \sin \delta_2}{h}$
θ_5	$-\omega_5$	$180^\circ + \omega_5$	$180^\circ - \omega_5$	ω_5
θ_6	$180^\circ - \omega_6$	$180^\circ - \omega_6$	$-\omega_6$	$180^\circ + \omega_6$

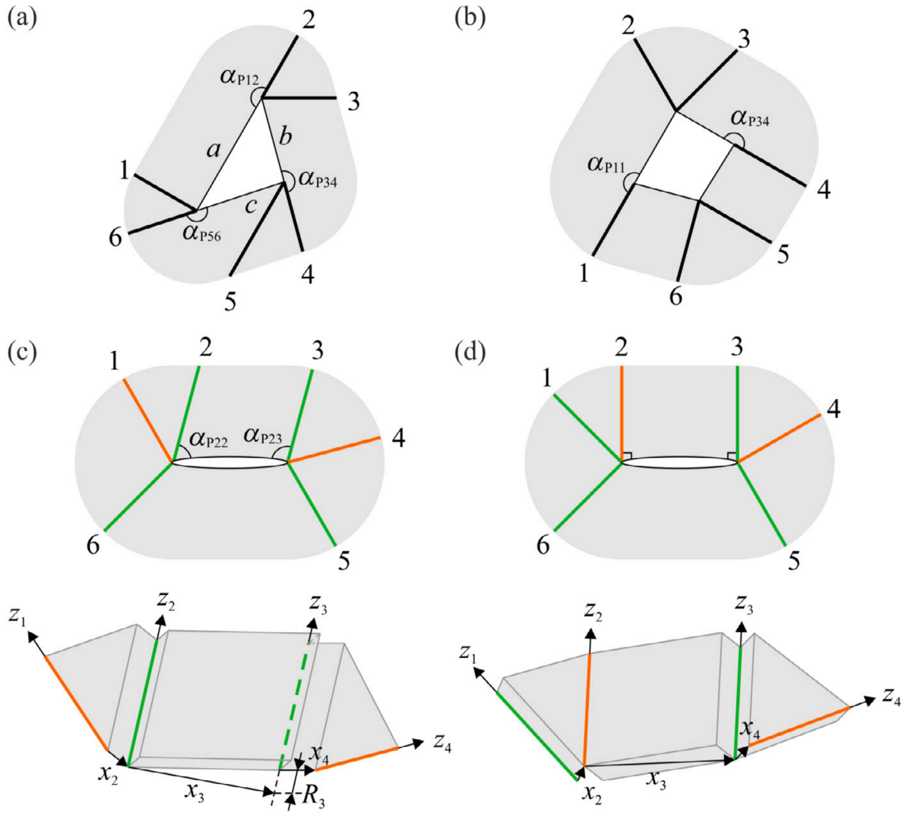

Fig. 4. Special fold arrangement. **(a)** and **(b)** Examples of intersecting folds to create zero joint offsets. **(c)** and **(d)** Examples of parallel folds to create zero joint offsets.

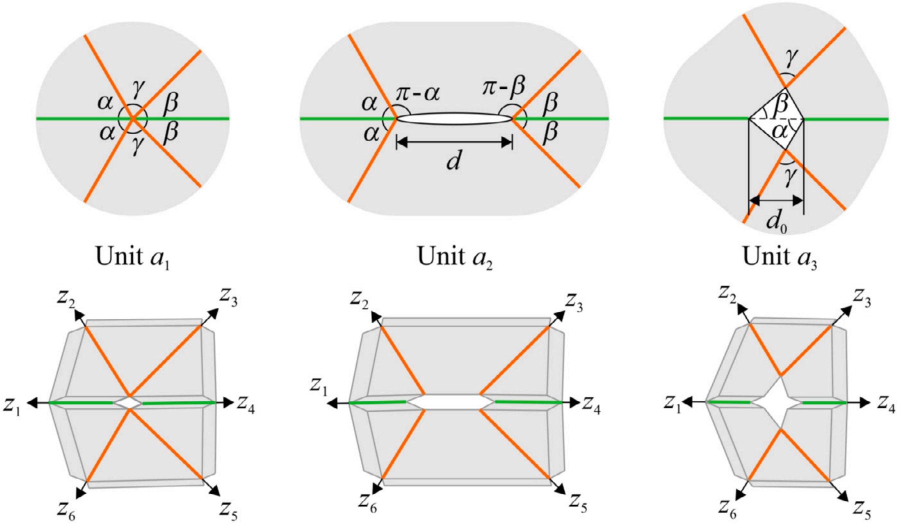

Fig. 5. The origami bases of Units a_1 - a_3 based on the plane-symmetric Bricard linkage and their 3D models.

after which other dihedral angles can be derived from the 4R spherical linkage.

To further illustrate where the third path happens, a special case when $\alpha = \beta$ is taken for Unit a_2. The corresponding dihedral angles in path 3 are

$$\begin{gathered}\omega_1 = \omega_4,\ \omega_2 = \omega_5,\ \omega_3 = \omega_6 \\ \tan\frac{\omega_1}{2} = \frac{d\tan\alpha}{2h} \\ \tan\frac{\omega_3}{2} = \frac{d\sin\alpha\tan\frac{\omega_2}{2}}{4h\cos^2\alpha\tan\frac{\omega_2}{2} - d\sin\alpha}\end{gathered} \tag{8}$$

Taking $\alpha = 60°$, the plots of path 1 and path 3 of Unit a_2 is given in Fig. 7. The new bifurcation point exists where two paths intersect, i.e., the unit is semi-folded. The point also varies along the ratio of slit length and panel thickness d/h. A simulated model in SOLIDWORKS is illustrated by the side.

2.2.2. Units based on the plane-symmetric Bricard linkage: type 2

Units b_1 - b_3 in Fig. 8 are also modelled as the plane-symmetric Bricard linkage, sharing exactly the same panels as Units a_1 - a_3, respectively. However, their fold arrangements have been changed,

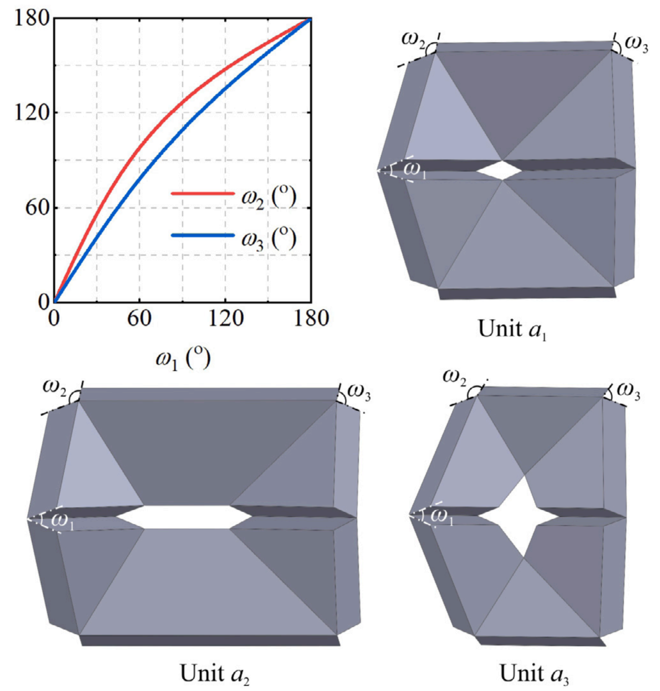

Fig. 6. Path 1 of Units a_1 - a_3 and associated 3D models. The unit is a flat array of thick panels when all angles are 0. Once fully folded, adjacent panels collide, yielding dihedral angles of 180°.

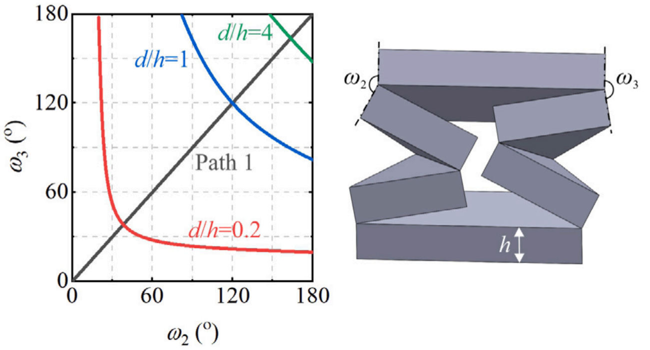

Fig. 7. Path 1 (black) and path 3 (coloured) of Unit a_2 when $\alpha = \beta = 60°$. The 3D models depict the configurations along path 3.

altering the geometric conditions as follows.

$$\begin{gathered} a_{12} = a_{23} = a_{34} = a_{45} = a_{56} = a_{61} = h \\ \alpha_{12} = 360° - \alpha_{61} = -\alpha \\ \alpha_{23} = 360° - \alpha_{56} = 180° - \alpha - \beta \\ \alpha_{34} = 360° - \alpha_{45} = -\beta \end{gathered} \tag{9}$$

$$R_1 = R_4 = 0,\ R_2 = -R_6 = -\frac{\sin\beta}{\sin(\alpha+\beta)}d,\ R_3 = -R_5 = \frac{\sin\alpha}{\sin(\alpha+\beta)}d$$

where the joint offsets remain the same as those in Eq. (4).

The closure equation of Units b_1 - b_3 as a plane-symmetric Bricard linkage is

$$\omega_2 = \omega_6,\ \omega_3 = \omega_5 \tag{10}$$

$$\tan\frac{\omega_1}{2} = -\frac{KI+L}{HI+J},\ \tan\frac{\omega_3}{2} = -\frac{2A_b}{I},\ \tan\frac{\omega_4}{2} = -\frac{OI+P}{MI+N} \tag{11}$$

for path 1,

$$I = -B_b - \sqrt{B_b^2 - 4A_bC_b} \tag{12}$$

for path 2,

$$I = -B_b + \sqrt{B_b^2 - 4A_bC_b} \tag{13}$$

where

$$A_b = h\sin(2\alpha)$$

$$B_b = 2d\sin(2\alpha)\sin\beta + 4h\sin(\alpha+\beta)\cot\frac{\omega_2}{2}$$

$$C_b = 3h\sin(2\alpha+2\beta) + \sin(2\beta)(h\cot\frac{\omega_2}{2} + 2d\sin\alpha)\cot\frac{\omega_2}{2}$$

$$H = -8h\sin^2\alpha\cos\beta\cot^2\frac{\omega_2}{2} - 2\sin(2\alpha)\sin\beta(h + d\sin\alpha\sin\omega_2)\csc^2\frac{\omega_2}{2}$$

$$\begin{aligned} J = & -8h^2\sin\alpha\sin(2\alpha)\sin(2\alpha+2\beta)\cot\frac{\omega_2}{2} \\ & -4h^2\sin\alpha\sin(2\alpha)\sin(2\beta)\cos\omega_2\csc^2\frac{\omega_2}{2}\cot\frac{\omega_2}{2} \\ & -8hd\sin^2\alpha\sin(2\alpha)\sin(2\beta)\cot^2\frac{\omega_2}{2} \end{aligned}$$

$$K = 4\sin\alpha\sin(2\alpha)(h\cos\beta\cot\frac{\omega_2}{2} + d\cos\alpha\sin\beta)$$

$$L = 4h^2\sin^2\alpha\sin(2\alpha+2\beta) + 4h\sin^2\alpha\sin(2\beta)(h\cot\frac{\omega_2}{2} + d\sin\alpha)\cot\frac{\omega_2}{2}$$

$$\begin{aligned} M = & \ 2h\sin(2\alpha)\sin(2\alpha+\beta) - 2\sin(2\alpha)\sin\beta(h\cot\frac{\omega_2}{2} + 2d\sin\alpha)\cot\frac{\omega_2}{2} \\ & -8h\sin^2\alpha\cos\beta\cot^2\frac{\omega_2}{2} \end{aligned}$$

$$\begin{aligned} N = & -4h^2\sin\alpha\sin^2(2\alpha)\cot\frac{\omega_2}{2} - 12h^2\sin\alpha\sin(2\alpha)\sin(2\alpha+2\beta)\cot\frac{\omega_2}{2} \\ & -4h\sin\alpha\sin(2\alpha)\sin(2\beta)(h\cot\frac{\omega_2}{2} + 2d\sin\alpha)\sin^2(2\alpha) \end{aligned}$$

$$\begin{aligned} O = & -8h\sin\alpha\sin(2\alpha)\cos\beta\cot\frac{\omega_2}{2} \\ & -4\sin(2\alpha)\cos\alpha\sin\beta(h\cot\frac{\omega_2}{2} + d\sin\alpha) \end{aligned}$$

$$\begin{aligned} P = & -8h^2\sin^2(2\alpha)\sin(2\alpha+2\beta) \\ & -4h\sin^2(2\alpha)\sin(2\beta)(h\cot\frac{\omega_2}{2} + d\sin\alpha)\cot\frac{\omega_2}{2} \end{aligned}$$

For Unit b_1 where the slit length $d = 0$, Eqs. (11)–(13) can be simplified.

For path 1,

$$\tan\frac{\omega_3}{2} = \frac{\sin(2\alpha)\tan\frac{\omega_2}{2}}{2\sin(\alpha+\beta) + \sqrt{Q}\tan\frac{\omega_2}{2}} \tag{14}$$

for path 2,

$$\tan\frac{\omega_3}{2} = \frac{\sin(2\alpha)\tan\frac{\omega_2}{2}}{2\sin(\alpha+\beta) - \sqrt{Q}\tan\frac{\omega_2}{2}} \tag{15}$$

where

$$Q = \frac{4\sin^2(\alpha+\beta) - \sin(2\beta)}{\tan^2\frac{\omega_2}{2}} - 3\sin(2\alpha)\sin(2\alpha+2\beta)$$

and

$$\begin{aligned} \tan\frac{\omega_1}{2} = & \frac{\sin\alpha\sin(\alpha+\beta)\sin\omega_3}{1 - \cos\omega_2(1-\cos\omega_3) - \cos(\alpha+\beta)\sin\omega_2\sin\omega_3} \\ & - \frac{-\cos\alpha(\sin\omega_2(1-\cos\omega_3) - \cos(\alpha+\beta)\cos\omega_2\sin\omega_3)}{1 - \cos\omega_2(1-\cos\omega_3) - \cos(\alpha+\beta)\sin\omega_2\sin\omega_3} \end{aligned} \tag{16}$$

$$\begin{aligned} \tan\frac{\omega_4}{2} = & \frac{\sin\omega_3 + \sin(\alpha+\beta)(\cot\alpha\csc\omega_2\cos\omega_3 - \tan\beta\cot\omega_2)}{\sec\beta(\cos\omega_3 + (\cos(\alpha+\beta)\cot\omega_2 - \cot\alpha\sin(\alpha+\beta)\csc\omega_2)\sin\omega_3)} \\ & - \frac{\cos(\alpha+\beta)(\cot\omega_2\cos\omega_3 + \cot\alpha\tan\beta\csc\omega_2)}{\sec\beta(\cos\omega_3 + (\cos(\alpha+\beta)\cot\omega_2 - \cot\alpha\sin(\alpha+\beta)\csc\omega_2)\sin\omega_3)} \end{aligned} \tag{17}$$

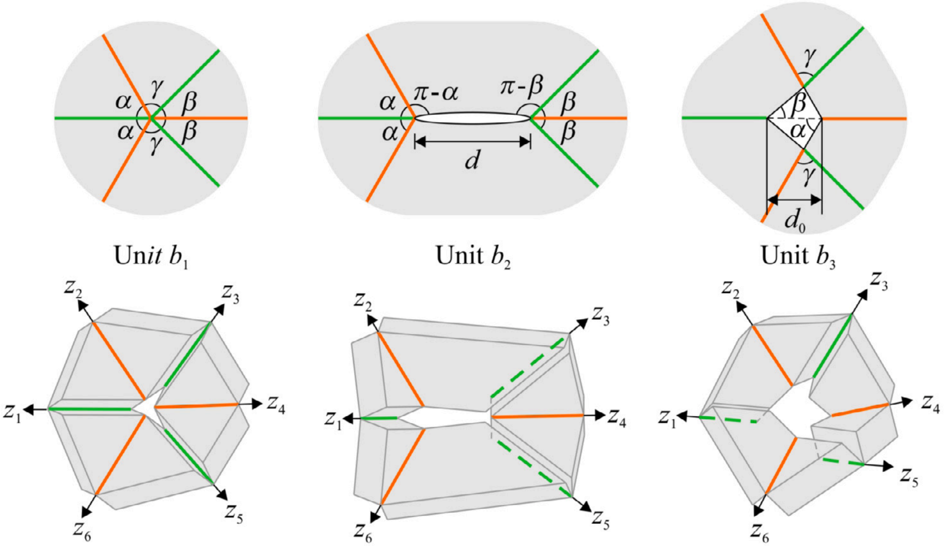

Fig. 8. The origami bases of Units b_1 - b_3 based on the plane-symmetric Bricard linkage and their 3D models.

According to Eqs. (10)–(17), the motions of Unit b_1 is independent from its panel thickness while those of Units b_2 and b_3 rely on the ratio d/h.

The same strategy for Units a_1 - a_3 is employed to examine additional bifurcations of Units b_1 - b_3. It is found that paths 1 and 2 are the only two motions of Units b_1 - b_3, which are switchable at the unfolded state of each unit. Taking $\alpha = 60°$, $\beta = 45°$, $d = 2h$ and $d_0 = 1.2h$, the kinematic behaviours of Units b_1 - b_3 are plotted in Fig. 9, respectively.

2.2.3. Units based on the line-symmetric Bricard linkage

In addition to the plane-symmetric Bricard linkage, the line-symmetric one can also be used to design morphing units as shown in Fig. 10. In Unit c_1, three pairs of aligned folds exist, giving $\gamma = \alpha + \beta - 180°$. Without changing the direction of these folds, a tilted slit and a parallelogram are introduced in Units c_2 and c_3 to maintain the line symmetry. Their geometric conditions are

$$\begin{gathered} a_{12} = a_{34} = a_{45} = a_{61} = h,\ a_{23} = a_{56} = 0 \\ \alpha_{12} = \alpha_{45} = -\alpha,\ \alpha_{23} = \alpha_{56} = 180° - \alpha - \beta,\ \alpha_{34} = \alpha_{61} = \beta \\ R_1 = R_4,\ R_2 = R_5,\ R_3 = R_6 \end{gathered} \tag{18}$$

The joint offsets of each unit are detailed as follows.

For Unit c_1,

$$R_1 = R_2 = R_3 = 0 \tag{19}$$

for Unit c_2,

$$R_1 = 0,\ R_2 = -\frac{\sin(\beta - \delta)}{\sin(\alpha + \beta)} d,\ R_3 = \frac{\sin(\alpha + \delta)}{\sin(\alpha + \beta)} d \tag{20}$$

and for Unit c_3,

$$R_1 \neq 0,\ R_2 \neq 0,\ R_3 \neq 0 \tag{21}$$

which means no three consecutive folds intersect at the same point on the 2D plane as depicted in Fig. 10.

The closure equations of Units c_1 - c_3 as a line-symmetric Bricard linkage are

$$\omega_1 = \omega_4,\ \omega_2 = \omega_5,\ \omega_3 = \omega_6 \tag{22}$$

$$\tan\frac{\omega_2}{2} = \frac{-B_{c1} - \sqrt{B_{c1}^2 - 4A_{c1}C_{c1}}}{2A_{c1}},\ \tan\frac{\omega_3}{2} = \frac{-B_{c2} + \sqrt{B_{c2}^2 - 4A_{c2}C_{c2}}}{2A_{c2}} \tag{23}$$

where

$$\begin{aligned} A_{c1} = {} & 2R_1 \sin\alpha \sin(\alpha + \beta) + R_2 \sin\alpha \sin\beta (1 + \cos\theta_1) \\ & + R_3 (1 - \cos\beta \cos(2\alpha + \beta) + \sin\beta \sin(2\alpha + \beta) \cos\theta_1) \\ & + 2h \cos\alpha \sin(\alpha + \beta) \sin\theta_1 \end{aligned}$$

$$B_{c1} = 2\sin(\alpha + \beta)(h(1 + \cos\theta_1) + R_3 \sin\beta \sin\theta_1)$$

$$C_{c1} = (1 + \cos\theta_1) \sin\beta (R_2 \sin\alpha + R_3 \sin\beta)$$

$$\begin{aligned} A_{c2} = {} & 2R_1 \sin\alpha \sin(\alpha + \beta) + R_3 \sin\alpha \sin\beta (1 + \cos\theta_1) \\ & + R_2 (1 - \cos\alpha \cos(\alpha + 2\beta) + \sin\alpha \sin(\alpha + 2\beta) \cos\theta_1) \\ & - 2h \cos\beta \sin(\alpha + \beta) \sin\theta_1 \end{aligned}$$

$$B_{c2} = -2\sin(\alpha + \beta)(h(1 + \cos\theta_1) - R_2 \sin\alpha \sin\theta_1)$$

$$C_{c2} = (1 + \cos\theta_1) \sin\alpha (R_2 \sin\alpha + R_3 \sin\beta)$$

According to [30], a general line-symmetric Bricard linkage would normally have two motion paths, However, when it comes to Units c_1 - c_3, one path is blocked and the remaining one in Eqs. (22)–(23) is defined as path 1. Assign the following geometric parameters to Units c_1 - c_3 as $\alpha = 60°$, $\beta = 45°$, $\delta = 15°$, $d = 2h$, $R_1 = -0.75h$, $R_2 = -1.6h$, and $R_3 = 1.32h$. The kinematic behaviour of each unit in path 1 is plotted in Fig. 11.

The three units are also examined regarding their kinematic bifurcations. Unit c_1 has three pairs of aligned folds. Considering its zero joint offsets, its motion paths are rewritten as

$$\omega_1 = \omega_4,\ \omega_2 = \omega_5,\ \omega_3 = \omega_6 \tag{24}$$

for path 1 of Unit c_1,

$$\tan\frac{\omega_2}{2} = \frac{1}{\cos\alpha} \tan\frac{\omega_1}{2},\ \tan\frac{\omega_3}{2} = \frac{1}{\cos\beta} \tan\frac{\omega_1}{2} \tag{25}$$

for path 2 of Unit c_1,

$$\omega_1 = \omega_2 = 0 \tag{26}$$

for path 3 of Unit c_1:

$$\omega_1 = \omega_3 = 0 \tag{27}$$

for path 4 of Unit c_1:

$$\omega_2 = \omega_3 = 0 \tag{28}$$

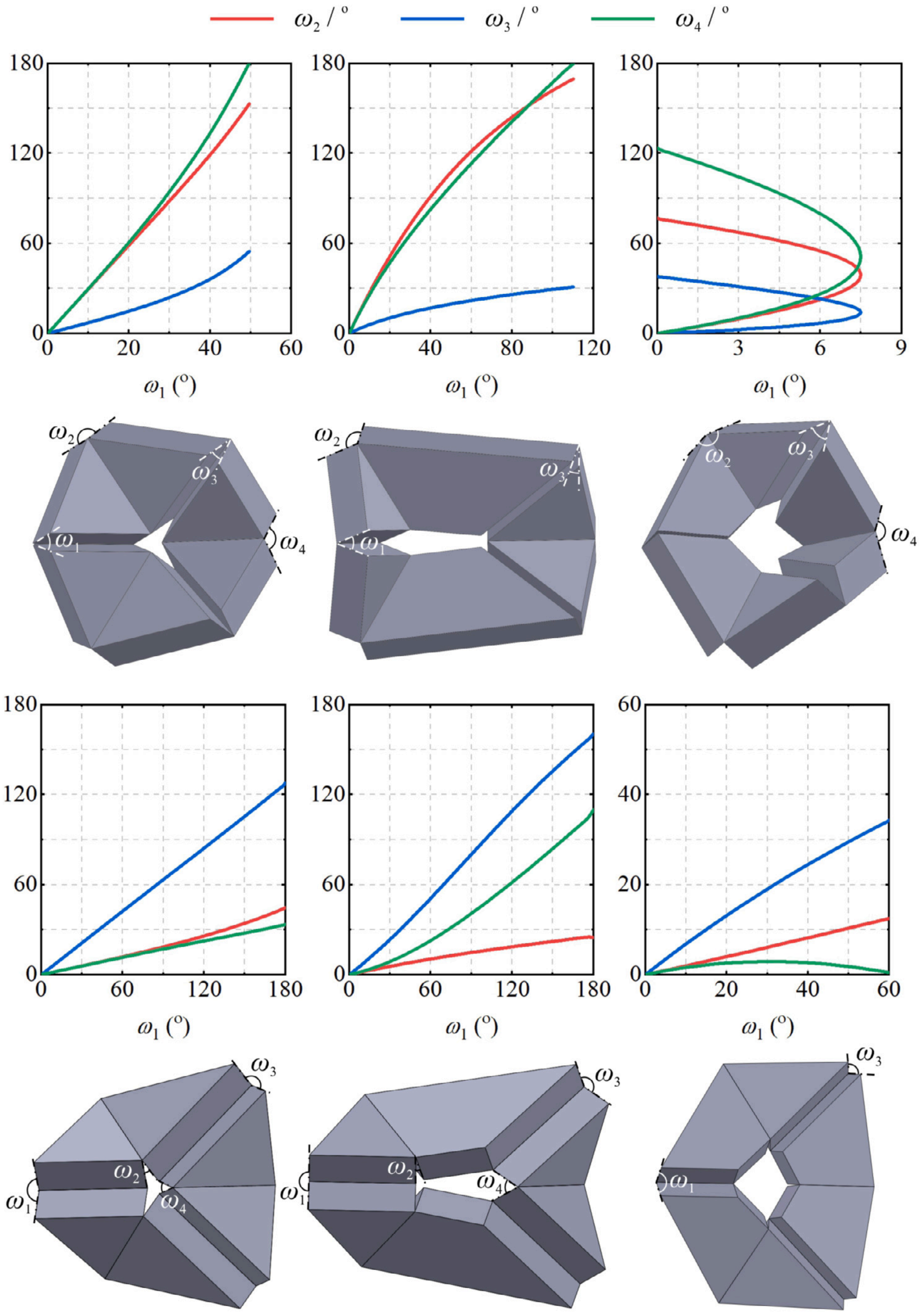

Fig. 9. Kinematic behaviour of Units b_1 - b_3 and associated 3D models. Path 1 of each unit is given at the top while path 2 is at the bottom.

Units c_2 and c_3 usually come with path 1 without bifurcations, whilst special geometric conditions could lead to additional motion paths. For instance, $\delta = 0$ or $\delta = \beta$ on Unit c_2 will lead to hinge-like motions as a result of aligned folds. Both units can also degenerate into 4R spherical linkages as detailed below.

For Unit c_2, if

$$\alpha = \beta,\ \delta = 0, \tag{29}$$

then

$$\tan\frac{\omega_1}{2} = \tan\frac{\omega_4}{2} = \frac{d\tan\alpha}{2h} \tag{30}$$

where the unit becomes the special case of Unit a_2 as discussed before. Folds 2, 3, 5, and 6 intersect at the same point while folds 1 and 4 are locked.

For Unit c_3, if

$$\begin{aligned} \tan\delta &= \frac{\sin(\alpha-\beta)}{2\cos\alpha\cos\beta} \\ \frac{d_1}{d_2} &= \frac{\sin(\alpha-\beta)\sin(\alpha-\delta)}{\sin(\alpha+\beta)\cos\alpha} \end{aligned} \tag{31}$$

then

$$\tan\frac{\omega_1}{2} = \tan\frac{\omega_4}{2} = \frac{d_1\tan\beta}{h(\tan\alpha-\tan\beta)} \tag{32}$$

where folds 1 and 4 are locked again into the values above.

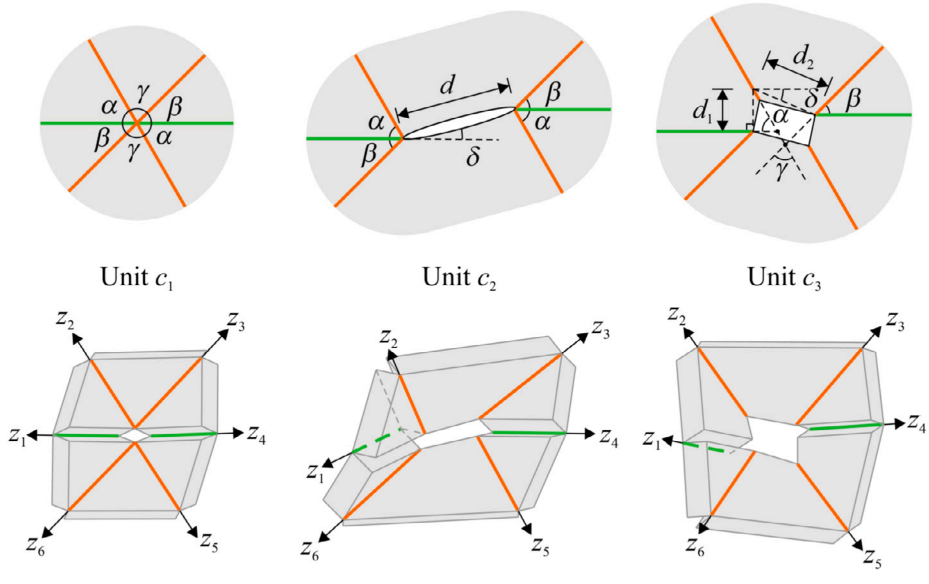

Fig. 10. The origami bases of Units c_1 - c_3 based on the line-symmetric Bricard linkage and their 3D models.

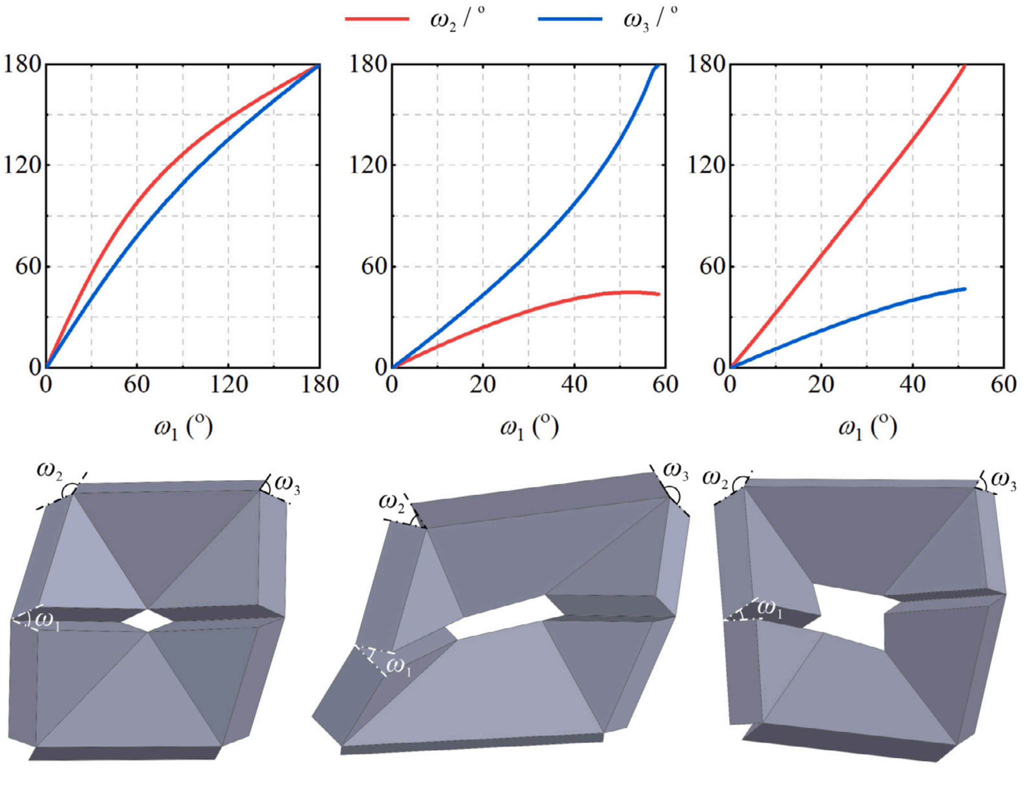

Fig. 11. Path 1 of Units c_1 - c_3 and associated 3D models.

2.2.4. Units based on other 6R spatial overconstrained linkages

Two more types of morphing units are found, which are based on the Wolhart 6R linkage and the Sarrus linkage, respectively.

As shown in Fig. 12 where $\alpha+\beta+\gamma=180^\circ$, Unit m_1 is modelled as the Wohlhart 6R linkage. Its geometric conditions are

$$a_{12}=a_{23}=a_{34}=a_{45}=a_{56}=a_{61}=h$$
$$\alpha_{12}=360^\circ-\alpha_{23}=-\alpha,\ \alpha_{34}=360^\circ-\alpha_{45}=-\beta,\ \alpha_{56}=360^\circ-\alpha_{61}=-\gamma$$
$$R_i=0,\ i=1,2,\dots,6 \tag{33}$$

When the geometric conditions in Eq. (33) are substituted into the closure equation in Appendix B, no symmetry is found among the dihedral angles and solving the equation can be challenging. So far, no analytical solutions of a general Wohlhart 6R linkage have been reported either. Nonetheless, when additional symmetry is added, i.e., $\alpha=\beta$ or $\alpha=\gamma$, Unit m_1 becomes a special case of Unit b_1, which is based on the plane-symmetric Bricard linkage. Its kinematic behaviours can thus be analysed from Eqs. (10) and (16)–(15).

Assigning $\alpha=\beta=\gamma=60^\circ$ to Unit m_1, its closure equation becomes

$$\omega_1=\omega_3=\omega_5,\ \omega_2=\omega_4=\omega_6 \tag{34}$$

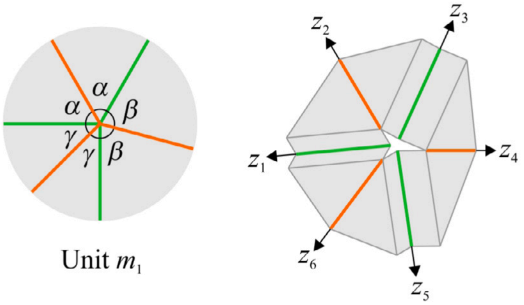

Fig. 12. The origami base of Unit m_1 based on the Wohlhart 6R linkage and its 3D model.

for path 1,

$$\tan\frac{\omega_2}{2}=\frac{\sin\frac{\omega_1}{2}}{2\cos\frac{\omega_1}{2}-\sqrt{3}} \tag{35}$$

for path 2,

$$\tan\frac{\omega_2}{2}=\frac{\sin\frac{\omega_1}{2}}{2\cos\frac{\omega_1}{2}+\sqrt{3}} \tag{36}$$

which are plotted in Fig. 13 along with simulated models. The kinematic bifurcation is at the unfolded state of the unit.

Unit m_2 shown in Fig. 14 is based on the Sarrus linkage, whose geometric conditions are

$$\begin{gathered}a_{12}=\sqrt{h^2+a^2\sin^2\delta_1},\ a_{23}=a_{56}=0\\ a_{34}=\sqrt{h^2+b^2\sin^2\delta_2},\ a_{45}=a_{61}=h\\ \alpha_{12}=\alpha_{34}=\alpha_{45}=\alpha_{61}=0,\ \alpha_{23}=\alpha_{56}=\alpha+\beta+\delta_1+\delta_2-180^\circ\\ R_1=a\cos\delta_1,\ R_2=R_3=0,\ R_4=-b\cos\delta_2\\ R_5=-\frac{c\sin(\beta+\delta_1)}{\sin(\delta_1+\delta_2-\gamma)},\ R_6=\frac{c\sin(\alpha+\delta_2)}{\sin(\delta_1+\delta_2-\gamma)}\end{gathered} \tag{37}$$

where $\frac{a}{\sin\alpha}=\frac{b}{\sin\beta}=\frac{c}{\sin\gamma}$ and $\alpha+\beta+\gamma=180^\circ$ must hold.

The closure equation of Unit m_2 gives

$$\sin\omega_6=\sin\omega_2-(1-\cos\omega_2)\frac{h_1}{h} \tag{38}$$

$$\tan\frac{\omega_3}{2}=\frac{-B_{m2}+\sqrt{B_{m2}^2-4A_{m2}C_{m2}}}{2A_{m2}} \tag{39}$$

$$\sin\omega_5=\sin\omega_3-(1-\cos\omega_3)\frac{h_2}{h} \tag{40}$$

$$\omega_1=\omega_2-\omega_6,\ \omega_4=\omega_3-\omega_5 \tag{41}$$

where

$$h_1=a\sin\delta_1,\ h_2=b\sin\delta_2$$

$$\begin{aligned}A_{m2}&=-4h_2^2\\&-(2h+h\cos\omega_2-h\cos\omega_6-h_1\sin\omega_2)(h\cos\omega_2-h\cos\omega_6-h_1\sin\omega_2)\end{aligned}$$

$$B_{m2}=4h_2(h-h\cos\omega_2+h\cos\omega_6+h_1\sin\omega_2)$$

$$\begin{aligned}C_{m2}\\&=-(h\cos\omega_2-h\cos\omega_6-h_1\sin\omega_2)(h\cos\omega_2-h\cos\omega_6-h_1\sin\omega_2-2h)\end{aligned}$$

Unit m_2 has only one motion path. By letting $a=b$ and $\delta_1=\delta_2=\delta$, Eqs. (38)–(41) are simplified as

$$\begin{gathered}\omega_4=\omega_1,\ \omega_3=\omega_2,\ \omega_5=\omega_6,\ \omega_2=\omega_1+\omega_6\\ \sin\omega_6=\sin\omega_2-\frac{a\sin\delta}{h}(1-\cos\omega_2)\end{gathered} \tag{42}$$

Taking $\alpha=\delta=60^\circ$ and $a=3h$, the kinematic behaviour of Unit m_2 is plotted in Fig. 14. The unit's movement is blocked when ω_6 returns to zero.

3. Morphing surfaces

The morphing units can be combined with shared folds to produce versatile motions. This section gives a few examples of tessellations and assemblies that demonstrate a wide range of motion possibilities.

3.1. Tessellations of morphing units

A tessellation is the covering of a surface using one or more geometric shapes with no overlaps or gaps [31]. This part details how the tessellation of morphing units can produce bending-, expanding-, and twisting-like motions similar to those in soft materials but with a single mobility.

3.1.1. Bending behaviours

Bending motions can be achieved by tessellating Units a_1 - a_3 as follows.

Fig. 15(a) illustrates a strip where two Units a_1 are connected. They are assigned with different geometric parameters, i.e., α_1, β_1, α_2, and β_2. The upper and bottom edges of the strip are parallel to the bottom folds. The shared fold, denoted by a star in the middle, passes the motion from one unit to the other. As such, the strip remains single mobility. According to Eq. (5), the use of slit or void does not influence the kinematic behaviours of these units as a Bricard linkage. The strip can thus be lengthened or shortened by changing one of Units a_1 to Unit a_2 or a_3, as shown in Figs. 15(b) and 15(c), respectively.

The strip in Fig. 15(a) can be extended vertically by adding an extra Unit a_1 with parameters α_3 and β_3 as shown in Fig. 15(d). The numbering of each fold is given, thereby representing the associated dihedral angles. The two units from the original strip give two angle inputs to the bottom unit with α_3 and β_3 via the shared folds, i.e., folds 15 and 32, folds 26 and 33. If the tessellation is mobile, the two angles must be compatible with the motion of the bottom unit, which is

$$\tan\frac{\omega_{33}}{2}=\frac{\cos\alpha_3}{\cos\beta_3}\tan\frac{\omega_{32}}{2} \tag{43}$$

where $\omega_{32}=\omega_{15}$ and $\omega_{33}=\omega_{26}$, as given by the shared folds.

The mathematical demonstration is as follows. Geometrically, we know

$$\alpha_3=\beta_1,\ \beta_3=\alpha_2,\ \omega_{14}=\omega_{21} \tag{44}$$

According to Eq. (5), we can obtain

$$\tan\frac{\omega_{i1}}{2}=\cos\alpha_i\tan\frac{\omega_{i2}}{2}=\cos\beta_i\tan\frac{\omega_{i3}}{2},\ i=1,\ 2 \tag{45}$$

$$\omega_{i1}=\omega_{i4},\ \omega_{i2}=\omega_{i6},\ \omega_{i3}=\omega_{i5},\ i=1,\ 2 \tag{46}$$

Eqs. (44)–(46) yields Eq. (43), making the motion of all units kinematically compatible. Thus, the tessellation is foldable and remains single-DoF.

Using such methods, various Units a_1 - a_3 can be tessellated to form large-scale surfaces with single mobility. Fig. 16 illustrates a general tessellation surface bending into an ellipse shape. The previously discovered origami and kirigami structures [18,24], which are composed of uniform-thickness panels, belong to a subset of the tessellation given here. In addition to the bending behaviour where each unit has a general Bricard linkage motion, the surface also has bifurcation paths caused by the alignment of bottom folds.

The bending curvature of such tessellations can be altered by tuning the geometric parameters of their constituent units. To obtain a regular-shaped curvature, identical panels are used to form the units. Fig. 17(a) depicts the tessellation of a triangle with interior angles α, β, and γ, which can roughly bend into a circular shape. When $\alpha=\beta$, the

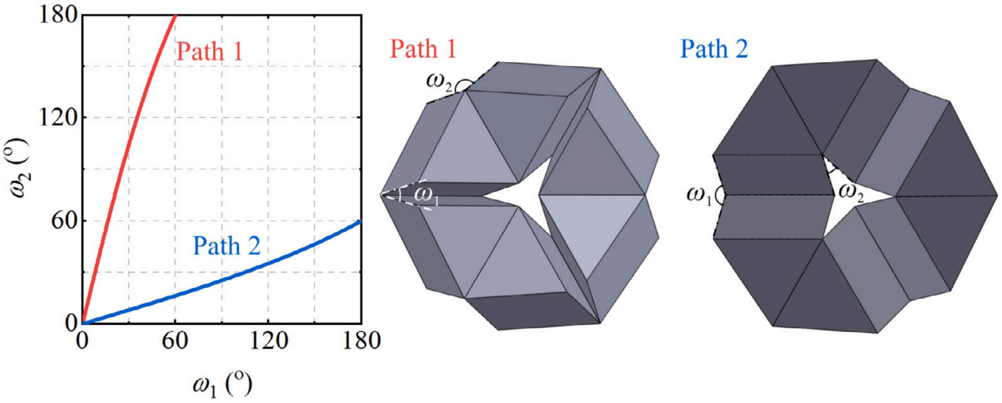

Fig. 13. Kinematic behaviours of Unit m_1 when all sector angles are 60°. 3D configurations of the two motion paths are also displayed.

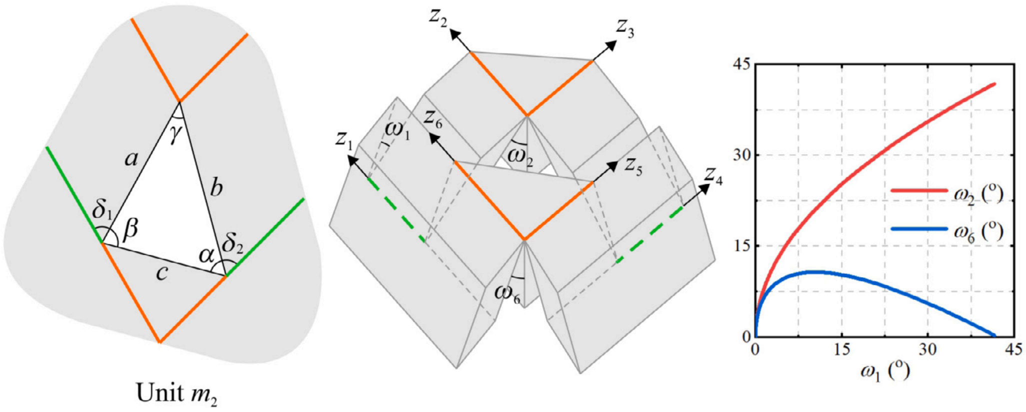

Fig. 14. The origami base of Unit m_2 based on the Sarrus linkage and its 3D model. Its kinematic motion paths when $\alpha = \beta = \gamma = \delta_1 = \delta_2 = 60°$ and $a = 3h$ are plotted by the side.

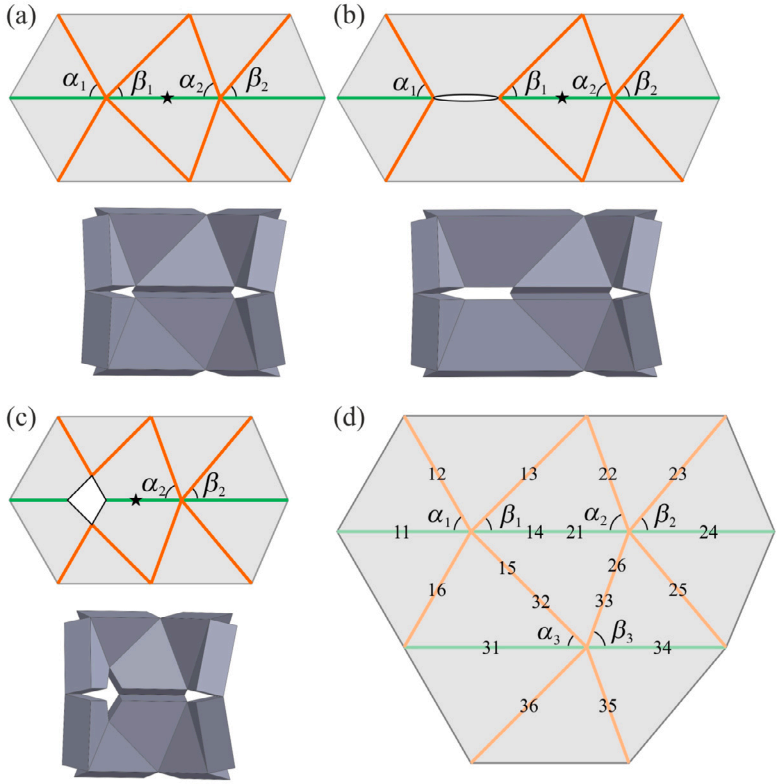

Fig. 15. Tessellations of Units a_1 - a_3 from Fig. 5 and their 3D models. **(a)**, **(b)**, and **(c)** Horizontal strips based on the connection of Units a_1 - a_3 **(d)** Vertical extension of a strip.

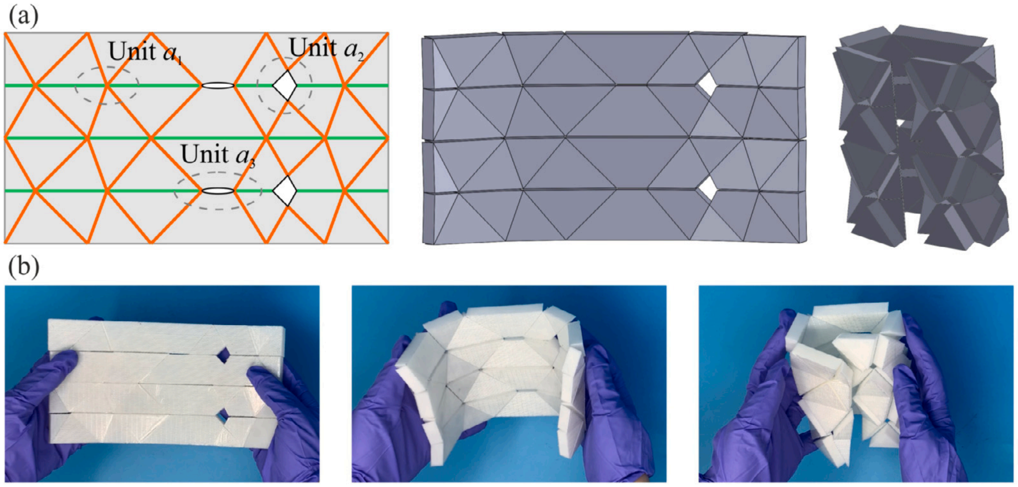

Fig. 16. The general tessellation of Units a_1 - a_3 and its bending motion. **(a)** The fold pattern and its simulated model in the flat unfolded and semi-folded states. **(b)** The bending motion on a physical prototype made from 3D-printed prisms (rigid panels) and glass fibre tapes (folds).

tessellation becomes Fig. 17(b), which is the thick-panel version of the Diamond pattern or the Yoshimura origami.

Identical trapezoids can also be used to create a tessellation of Units a_2 with slits. A special case is illustrated in Fig. 17(c), where the trapezoid is isosceles. The surfaces have single DoF when all units undergo the general motion of a Bricard linkage but could also move into other configurations due to the aligned folds. Theoretically, the surface can shift from bending to twisting when each unit degenerates into a 4R spherical linkage at the semi-folded state, as detailed in Eq. (8). However, this turns out physically impossible due to panel collisions.

3.1.2. Expanding behaviours

Identical Units b_1 - b_3 can be connected into a two-layered surface capable of expanding. Taking Unit b_1 as an example, the tessellation method is as follows.

The patterns of Units $b_{1.1}$ and $b_{1.2}$, composed of identical triangular prisms, are given in Fig. 18. Their geometric parameters have the following relationship: $\alpha_1 = \beta_2 = \alpha$, $\alpha_2 = \beta_1 = \beta$, and $\gamma_1 = \gamma_2 = \gamma$. Hence, the two units are kinematically equivalent but positioned upside down. When Units $b_{1.1a}$ and $b_{1.2}$ are in their paths 1 and 2 respectively, their finished configurations are the same. This enables three Units $b_{1.1}$ to be connected with Unit $b_{1.2}$ by three pairs of edges highlighted in Fig. 18. Each pair of connections plus folds between the pairs form a planar 4R linkage. The connection also blocks the bifurcation paths as a result of physical interference. Hence, these connected units remain single-DoF and become bifurcation-free.

More Units b_1 can be joined to form a two-layered tessellation as shown in Fig. 19. The constituent units in Fig. 19(a) are derived from a general triangle base. The tessellation in Fig. 19(b) is based on equilateral triangles, making the individual unit also a special case of Unit m_1. The input angle ω_1, marked in Fig. 18, increases from 0 to 180° to illustrate the expanding motions.

The tessellations originating from Unit b_1 are possible as a result of the plane symmetry among dihedral angles and the alternative top and bottom fold arrangements on each unit. Therefore, Unit b_2 or Unit b_3, which has similar properties, can be connected in the same way. Their examples are not detailed here.

3.1.3. Twisting behaviours

Units c_1 - c_2 exhibit line (or rotational) symmetry in the folding process, which is commonly observed in twisting structures. Identical units are connected to form large-scale tessellations as shown in Figs. 20–22, some of which clearly show twisting behaviours. The tessellation process is detailed below.

Fig. 20 is a tessellation of Unit c_1, where each unit based on triangles with α, β and γ as the internal angles. The kinematic motion is passed from one unit to another via the shared folds, and thus the mechanism remains single mobility when all units are in the general motion path of a Bricard linkage. In the meantime, the mechanism also has multiple DoFs at the flat state due to aligned folds.

Unit c_2 or Unit c_3 can also be arranged similarly. The tilted slits or voids will destroy aligned folds, thereby eliminating hinge-like motion paths on such tessellations. For instance, Fig. 21 illustrates an example of Unit c_2 tessellation. The bases consist of identical quadrilaterals. A more evident twisting behaviour is observed and the motion is bifurcation-free.

Unit c_3 with a parallelogram void can also be tessellated as depicted in Fig. 22. Before assembling, the unit's central void shape is modified into a hexagon, which would not change the unit's kinematic behaviours, as depicted in Fig. 22(a). The hexagon's sides are parallel to the respective folds of the unit. The opposite sides of the hexagon are also equal. Then each panel of the unit is replaced by the same hexagon as the central void, making the unit ready to be tessellated into a surface shown in Fig. 22(b). Note that none of the folds on Unit c_3 are aligned, and thus, the bifurcation paths caused by colinear folds are removed. The physical prototype of the tessellation and its folding process are illustrated in Fig. 22(c).

3.2. Assemblies of morphing units

In addition to full-surface tessellations capable of basic motions, the morphing units can be assembled in a less systematic way to produce complex behaviours as another type of morphing surface. Regardless of the infinite permutations, this section only presents a limited number of surfaces that can undergo complex movements and morph into functional configurations.

3.2.1. Wrapping and curling behaviours

Wrapping behaviours can be achieved on a circular assembly of Units a_1 or Units c_1 when they have both line and plane symmetry. Three-unit, four-unit, and five-unit assemblies are illustrated in Fig. 23. The corner panels of each assembly can wrap around the central base when the units are in their respective path 1. The single-DoF feature is preserved due to shared common folds whilst each assembly also possesses kinematic bifurcations as a result of aligned bottom folds. Notably, the four-unit assembly has also been used as a gripper backbone to explore its functionalities of grasping and in-hand manipulation [32,33]. The assembly can also be regarded as a unit and then tessellated into mechanical metamaterials with negative Poisson's ratio [34].

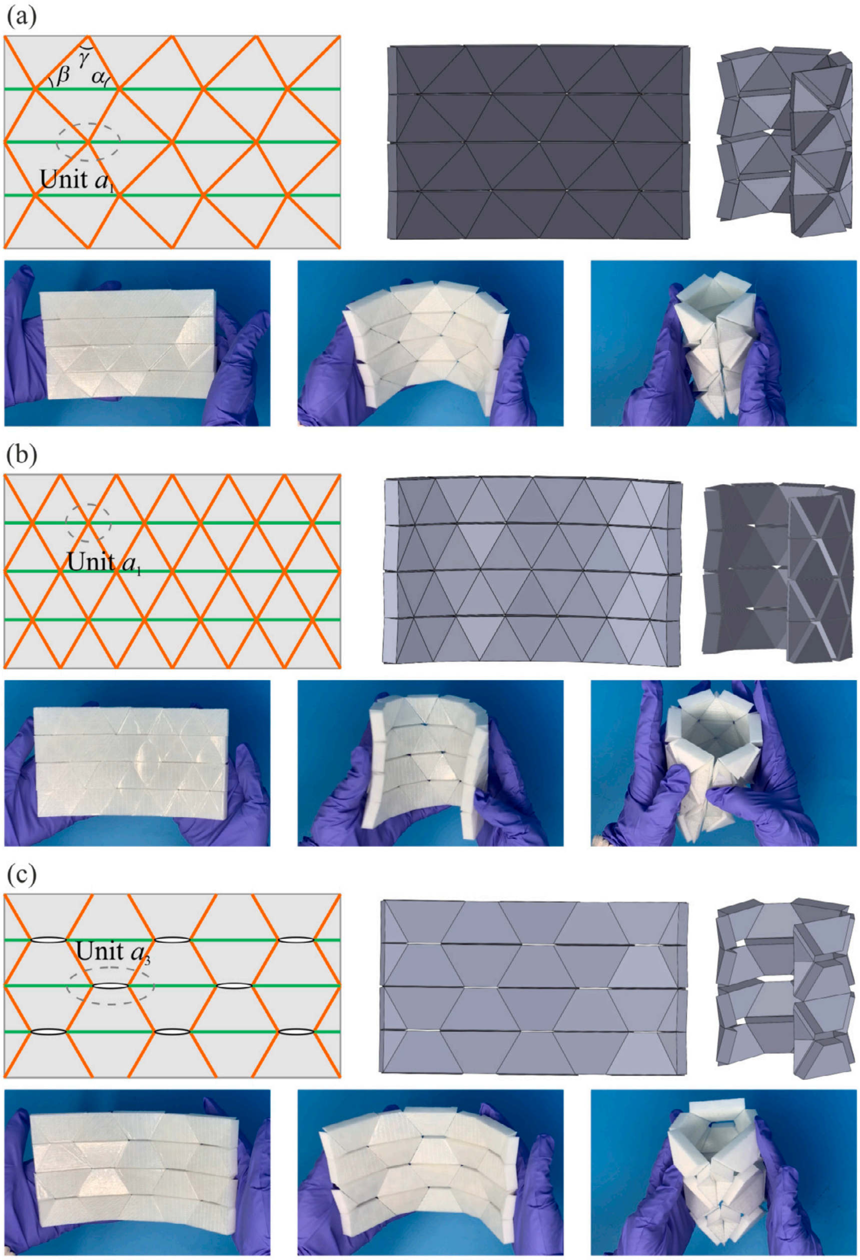

Fig. 17. Tessellations of identical panels to achieve regular bending shapes. The panels' bases include **(a)** general triangles, **(b)** isosceles triangles, and **(c)** isosceles trapezoids. Repeated individual units of each tessellation are highlighted.

The chain-like assembly shown in Fig. 24 can generate curling motions. The surface is composed of two types of morphing units, i.e., Units a_2 and b_1. The pattern is symmetric about its central axis, as denoted by the dashed line. The units repeat one after another along the chain.

When all Units a_2 and b_1 are in their respective motion path 1, a curling behaviour of the chain is produced, whose cross-sectional view is illustrated in Fig. 24(b) left. When Units a_1 remain in the same path and all Units b_1 switch to their motion path 2, another curling motion is generated in Fig. 24(b) right. The surface has been exploited to mimic a millipede's behaviour and achieve robot reconfiguration [35,36]

3.2.2. Functional configurations

Assemblies of morphing units can also provide a straightforward way to turn an array of uniform-thickness panels into stable 3D configurations, with the aid of a few fixtures. For instance, Unit b_1 or m_1 can be turned into a hill-like shape as shown in Fig. 25(a), where each panel is based on equilateral triangles. The bending surface can morph into a cylinder as shown in Fig. 25(b), where the units on both sides are connected appropriately. Similarly, the curling surface can also form a wheel-like closed-loop configuration which is depicted in Fig. 25(c). Each finishing configuration is a stable structure rather than a mobile mechanism as the only DoF is restricted by the connected panels. This approach is transferrable to large-scale construction projects.

In addition to the aforementioned surfaces, arbitrary units can be combined to produce more complicated shapes. For example, a cylindrical configuration can also be achieved by an array of parallelograms and triangles as shown in Fig. 26(a), where each unit is essentially Unit m_2. A spherical configuration is possible through the arrangement of Units a_1 and b_1, as shown in Fig. 26(b). It is actually impossible to enumerate all potential shapes as the possibilities are infinite.

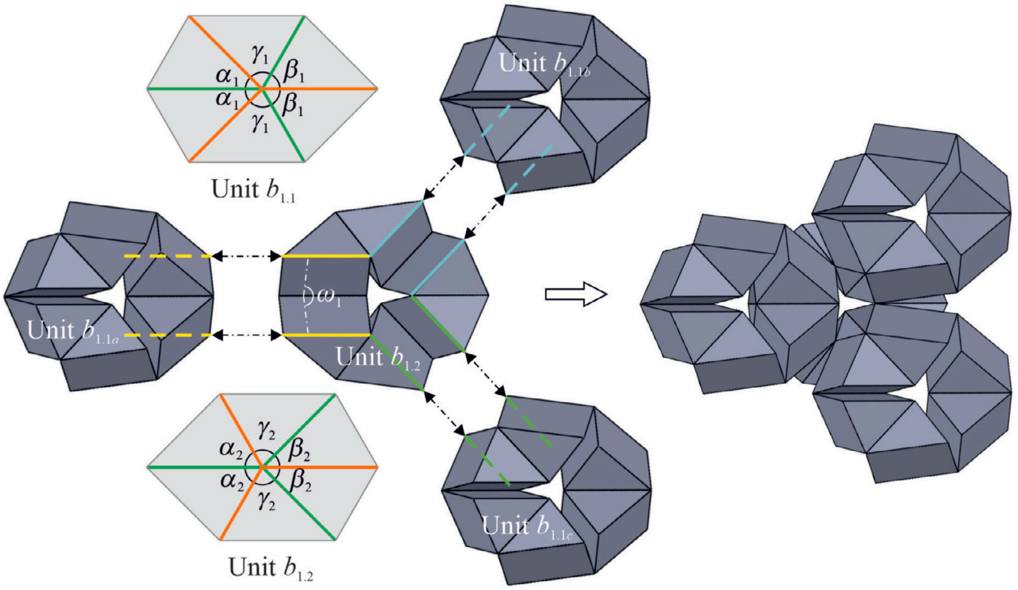

Fig. 18. Assemblies of Units b_1 from Fig. 8 for expansion. ω_1 of Unit $b_{1.2}$ is taken as input.

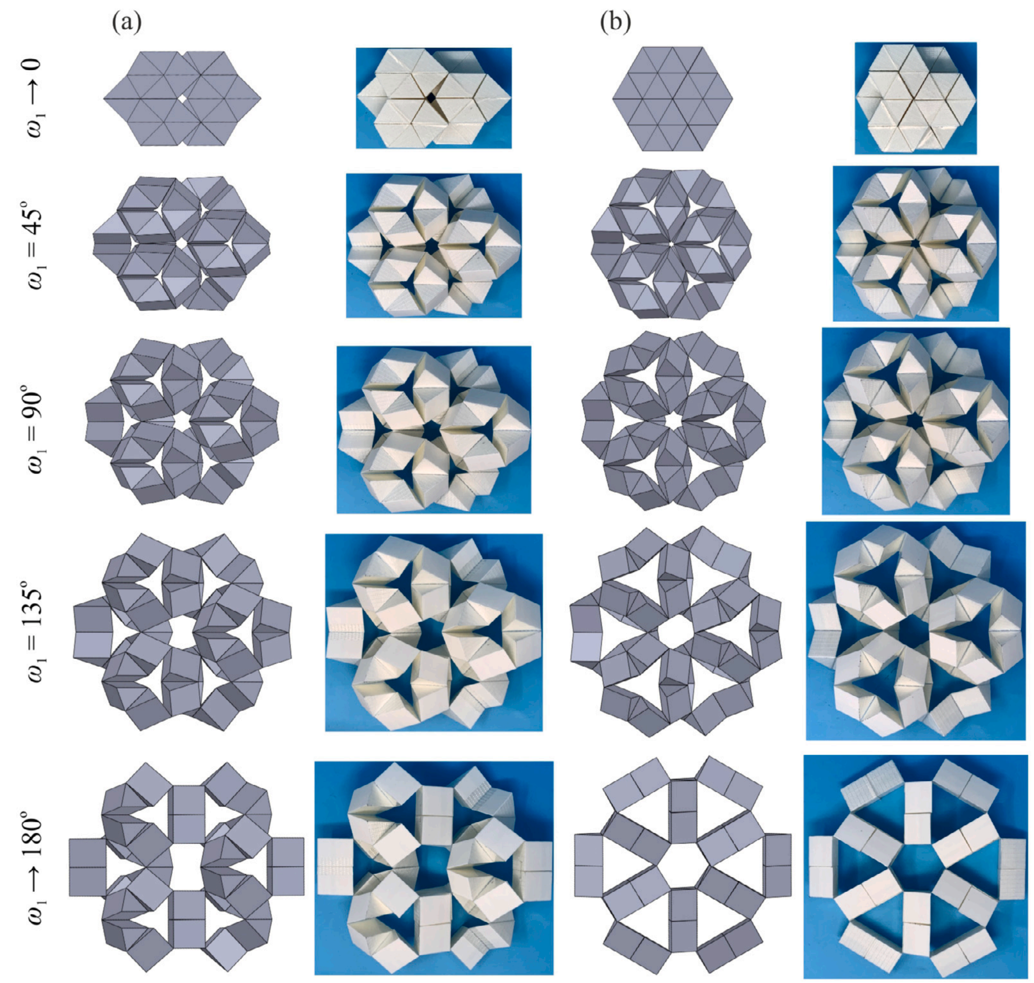

Fig. 19. Expanding behaviours on the tessellations of Units b_1 where the two-layered surfaces are based on **(a)** general triangles with interior angles as 45°, 75°, and 60°, and **(b)** equilateral triangles. The latter has a more uniform expansion.

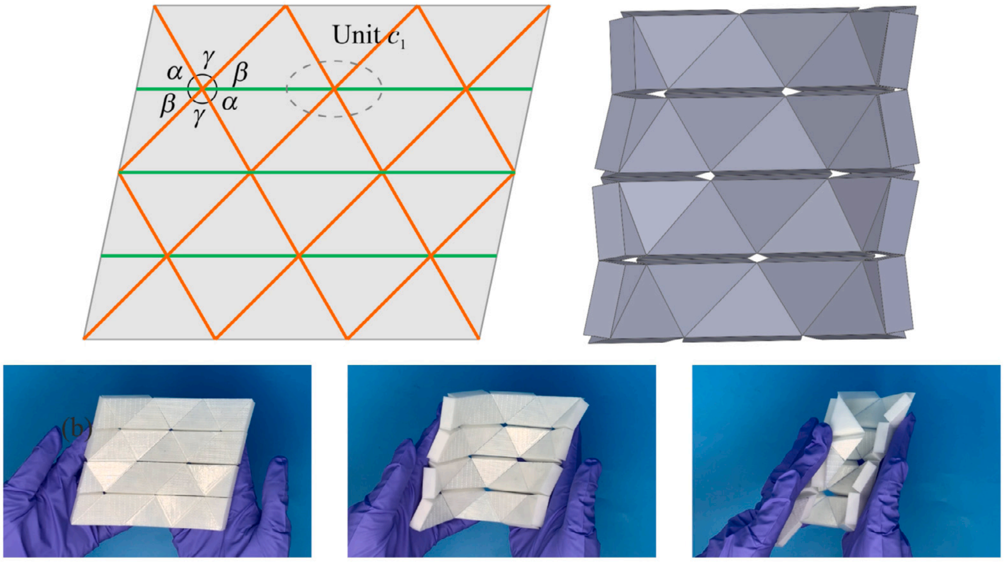

Fig. 20. Tessellation of repeated Units c_1 from Fig. 10. The surface is based on identical triangle panels, where $\alpha = 60°$, $\beta = 45°$, and $\gamma = 75°$. The fold pattern, simulated model, and physical prototypes are all displayed.

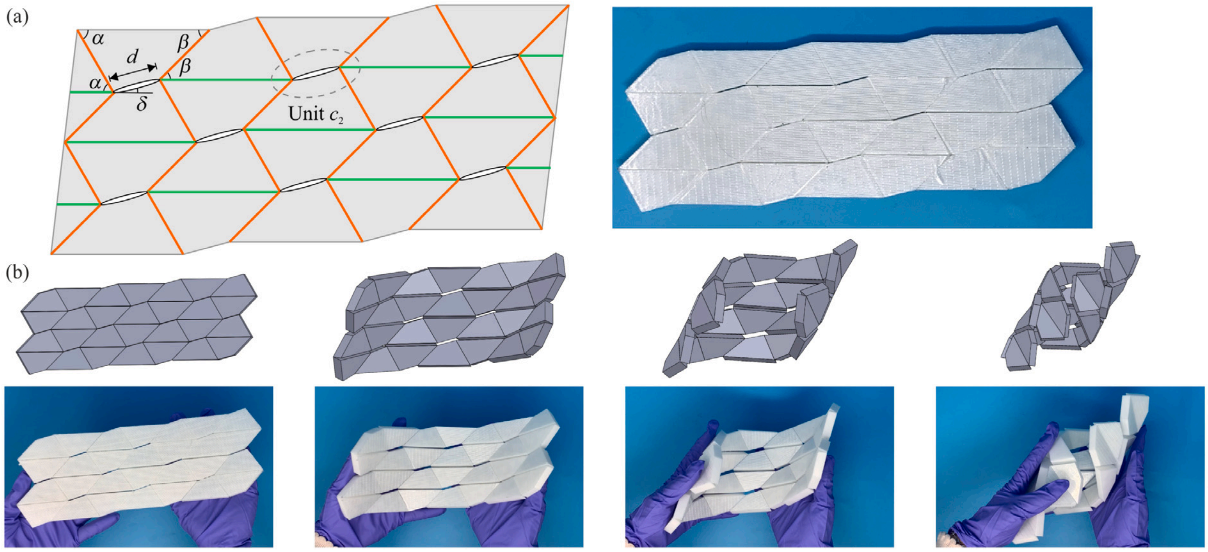

Fig. 21. Tessellation of repeated Units c_1 from Fig. 10. The surface is based on identical triangle panels, where $\alpha = 60°$, $\beta = 45°$, and $\gamma = 75°$. The fold pattern, simulated model, and physical prototypes are all displayed.

4. Discussions

4.1. Morphing units

Using a systematic design approach, i.e., mapping all 6R spatial overconstrained linkages with thick-panel origami, a complete library of morphing units is uncovered and summarised in Table 3. Each unit is made from uniform-thickness panels and possesses a single mobility. Among all the units, Units a_1 and c_1, Units a_2 and c_2, and Units b_1 and m_1 are interchangeable with each other under certain geometric conditions. Some units are bifurcation-free with only one path, whilst the rest have at least two sets of motions. In addition to the general 6R overconstrained linkage motion, other paths are caused by either aligned folds to produce hinge-like motions, or the intersection of four folds to create a spherical linkage. The units are ready to be assembled to create large-scale morphing surfaces.

It should also be noted that some units or their special cases have already been reported in the literature. In particular, the constituent units of the uniform-thickness Diamond pattern developed by Zhang and Chen [18] can be regarded as Unit a_1. In addition, the units from a kirigami tessellation based on the Waldron hybrid linkage found by Wang et al. [24] are equivalent to Unit a_2. [37] later reported each unit's kinematic bifurcations using the predictor–corrector numerical method, to which the analytical solutions in this paper are complementary. A special case of Unit m_1 was taken as a three-fold symmetric Bricard linkage [38]. Our work not only covers these designs but also provides more varieties that were previously neglected.

4.2. Morphing surfaces

Soft-material-like behaviours such as bending, expanding, and twisting are realised by tessellating some units into morphing surfaces. In real-world applications, identical panels are often desired for fabrication simplicity. Given this fact, a new categorisation of identical basic shapes, i.e., triangles, quadrilaterals, and hexagons, is given in Table 4, to form versatile morphing surfaces.

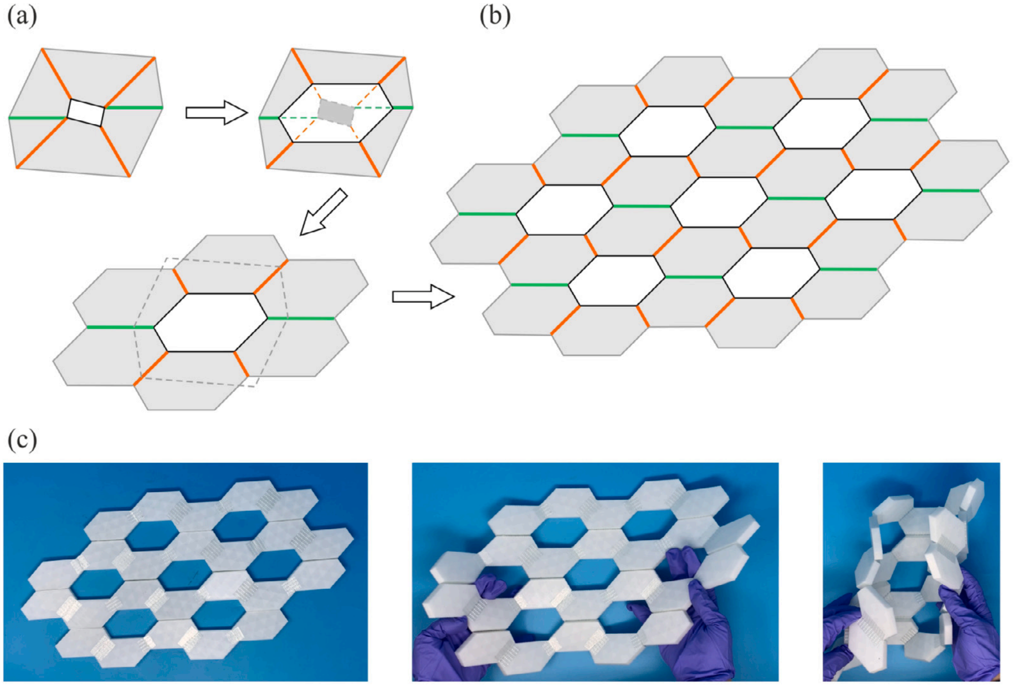

Fig. 22. Tessellation of repeated Units c_3 from Fig. 10 and their modifications into an assembly of identical hexagon panels. **(a)** and **(b)** Single unit modification process and its tessellation pattern. **(c)** Folding process of the physical prototype.

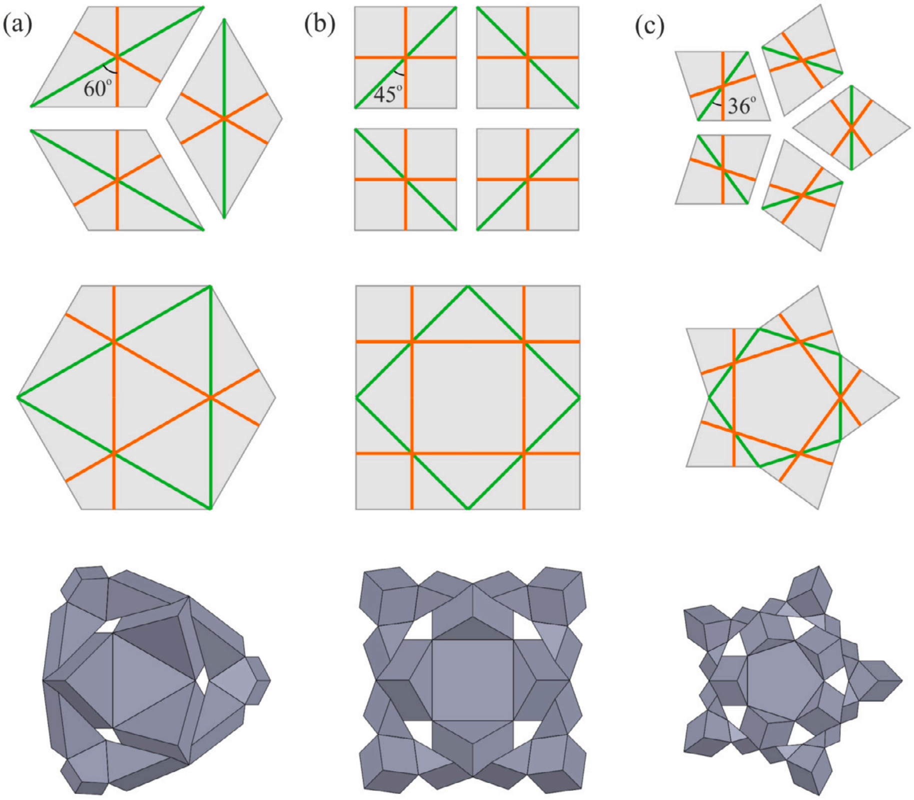

Fig. 23. Wrapping motions of **(a)** three-unit, **(b)** four-unit, and **(c)** five-unit assemblies.

Compared to the properties of morphing units in Table 3, it is found that some surfaces, i.e., the ones capable of expanding, have a smaller number of bifurcations than their constituent units. This is because new physical interferences are introduced to remove one of the original motion paths. Some twisting surfaces have only one DoF as a result of their bifurcation-free units.

Note that QVP-based morphing units, i.e., Units a_3, b_3, and m_2, are not well included in Table 4 except for Unit c_3. However, this does

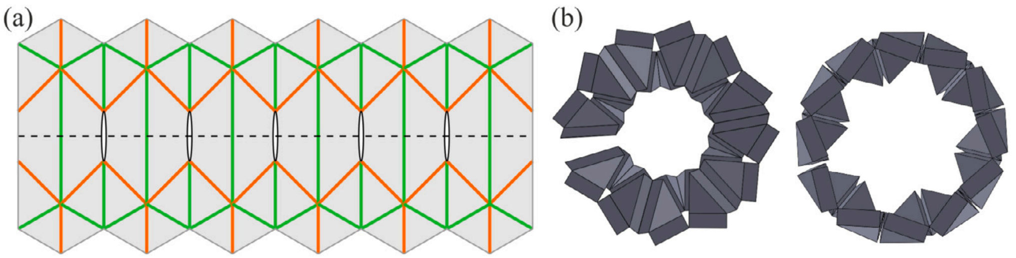

Fig. 24. Design of a curling surface. **(a)** Top view of the origami pattern. **(b)** and **(c)** Cross-sectional views of two curling configurations.

Table 3
Summary of morphing units and their kinematic properties.

Unit	Base	Linkage	Number of motion paths	Bifurcation point
a_1	SVP	Plane-symmetric Bricard linkage	2[*]	Flat
a_2	SSP		3	Flat, semi-folded
a_3	QVP		2	Flat
b_1	SVP		2	Flat
b_2	SSP		2	Flat
b_3	QVP		2	Flat
c_1	SVP	Line-symmetric Bricard linkage	4	Flat
c_2	SSP		1[**]	Flat, semi-folded
c_3	QVP		1[***]	Semi-folded
m_1	SVP	Wolhart 6R linkage	2	Flat
m_2	TVP	Sarrus linkage	1	None

[*] The number of motion paths rises to 4 when Unit a_1 has line and plane symmetry, i.e., $\alpha = \beta$.
[**] The number of motion paths in Unit c_2 rises to 2 when $\delta = 0$ or $\delta = \beta$, and rises to 3 when $\delta = 0$ and $\alpha = \beta$. Both cases have aligned folds and the latter is a special case of Unit a_2.
[***] The number of motion paths rises to 2 when Unit c_3 meets the condition set in Eq. (31).

Table 4
Basic shapes and their tessellation properties.

Shape	Requirement	Unit	Motion of tessellated surface	Number of motion paths
Triangle	General	a_1	Bending	>1
		b_1	Expanding	1
		c_1	Twisting (imperceptible)	>1
	Equilateral	a_1/c_1	Bending	>1
		b_1/m_1	Expanding (isotropic)	1
Quadrilateral	General	c_2	Twisting (obvious)	1
	Trapezoid	a_2	Bending	>1
		b_2	Expanding	1
Hexagon	Equal and parallel opposite sides	c_3	Twisting (imperceptible)	1

not mean that those units cannot be used for surface tessellations as this section only aims to give a few examples to achieve bending, expanding, and twisting motions. It should be emphasised that the possibilities are unlimited and all units in Table 3 can be combined according to the specific needs, as exemplified by the assemblies of morphing units. Motions can be passed via shared folds, producing complex behaviours with low DoFs.

5. Conclusions

Roboticists have vastly used origami structures as skeletons for desirable motions. Origami engineers also make efforts to design novel structures for shape-changing. Despite the substantial progress and promising potential, a particular type of origami, i.e., thick-panel origami, is yet accessible to the robotics community, due to a few barriers. To address the research gaps, this work proposes a systematic approach to designing kinematic morphing units inspired by thick-panel origami. A library of morphing units is achieved by an exhaustive mapping between thick-panel origami and 6R spatial overconstrained linkages. The obtained units are capable of versatile motions, whose kinematic behaviours are analysed in detail. To make the results more inclusive to the roboticists, we also give a series of examples which combine morphing units by tessellation or assembly, yielding morphable surfaces that can bend, expand, twist, or undergo complex behaviours. With a proper selection and combination of morphing units from the library, the surfaces' shape-changing possibilities are

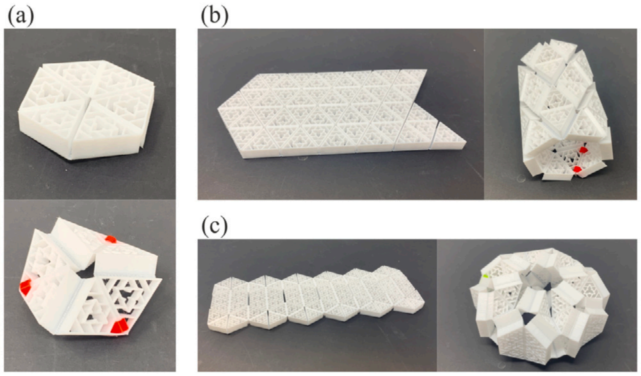

Fig. 25. Units and surfaces morph from flat configurations to provide 3D structures, which are based on **(a)** Unit b_1 or m_1, **(b)** the bending surface in Fig. 17(b), and **(c)** the curling surface composed of equilateral triangles and isosceles trapezoids. The coloured parts are 3D-printed fixtures.

unlimited. Notably, all the morphing surfaces retain single mobility as their constituent units, whilst bifurcations may accumulate or be eliminated. The work paves the way to exploit TPO in the design of future origami robots.

CRediT authorship contribution statement

Chenying Liu: Writing – review & editing, Writing – original draft, Visualization, Validation, Software, Resources, Project administration, Methodology, Investigation, Formal analysis, Data curation, Conceptualization. **Fufu Yang:** Writing – review & editing, Methodology, Investigation, Formal analysis. **Perla Maiolino:** Writing – review & editing, Supervision, Resources, Funding acquisition, Conceptualization. **Zhong You:** Writing – review & editing, Validation, Supervision, Resources, Project administration, Methodology, Investigation, Formal analysis, Conceptualization.

Declaration of competing interest

The authors declare that they have no known competing financial interests or personal relationships that could have appeared to influence the work reported in this paper.

Acknowledgments

We gratefully acknowledge the support of the EPSRC Programme Grant “From Sensing to Collaboration” (EP/V000748/1).

Appendix A. Pattern selection

The most general origami base should be composed of both creases and slits. For TPO design, each base can be modelled as a spatial linkage where all creases are treated as revolute joints. Here we only focus on six-crease bases as their equivalences are 6R spatial overconstrained linkages, which are most abundant in number and relatively less studied for TPO design.

For the most simple base without a slit, all creases should intersect at a single vertex as shown in the SVP in Fig. 1(a). If the creases intersect at more than one vertex, slits must exist to connect these vertices. In the meantime, a vertex indicates that at least two creases have met here. The cases are thus listed as follows.

A single slit connects two vertices. The six creases can be distributed equally on the two vertices as shown in the SSP in Fig. 1(b). Another possible base is having two creases meet at one vertex and leaving the other four intersecting at the other vertex. It is kinematically equivalent to the pattern in Fig. 4(b) and later demonstrated impossible to be mobile as TPO units. Hence, this pattern is excluded from the four selected bases.

Table B.5
Kinematic parameters of a joint.

z_i	Coordinate axis along the revolute joint i
x_i	Coordinate axis common normal from z_{i-1} to z_i
y_i	Coordinate axis determined by the right-hand rule
θ_i	Rotation angle from x_i to x_{i+1} about z_i, revolute variable of joint i
$\alpha_{i(i+1)}$	Rotation angle from z_i to z_{i+1} about x_{i+1}, link twist of link$_{i(i+1)}$
$a_{i(i+1)}$	Distance between z_i and z_{i+1}, link length of link$_{i(i+1)}$
R_i	Distance between x_i and x_{i+1}, positive along z_i, offset of joint i

When there are three vertices, a triangle void composed of three slits can help to connect them together. Since there are six creases in total and at least two creases are needed to create a vertex, the only possibility is to equally distribute the creases among three vertices, as shown in the TVP in Fig. 1(c).

Whilst the SVP, SSP, and TVP have covered the majority of bases, special cases can occur when some creases are parallel to each other. Hence, a base with a quadrilateral void, i.e., the QVP, is introduced in Fig. 4(d) to cover special cases, where a vertex no longer requires two creases to meet. Whilst the current crease distribution among four vertices is 1-2-1-2, it is not difficult to demonstrate that any other distribution is essentially the same as this one by adjusting the void shape.

Appendix B. DH notations and closure equations

To model thick-panel origami, researchers often employ a matrix method with DH notations [39]. The method standardises the setup of a coordinate system at each joint in a linkage presented in Fig. B.27. The kinematic parameters that define the joint and the two links it connects are given in Table B.5.

A vertex in rigid origami is modelled as a single-loop closed kinematic chain of n links, whose closure equation is

$$T_{21}T_{32}...T_{1n} = I_4 \tag{B.1}$$

where I_4 is a 4 × 4 identity matrix.

The transformation matrix $T_{(i+1)i}$ is

$$T_{(i+1)i} = \begin{bmatrix} \cos\theta_i & -\cos\alpha_{i(i+1)}\sin\theta_i & \sin\alpha_{i(i+1)}\sin\theta_i & a_{i(i+1)}\cos\theta_i \\ \sin\theta_i & \cos\alpha_{i(i+1)}\sin\theta_i & -\sin\alpha_{i(i+1)}\sin\theta_i & a_{i(i+1)}\sin\theta_i \\ 0 & \sin\alpha_{i(i+1)} & \cos\alpha_{i(i+1)} & R_i \\ 0 & 0 & 0 & 1 \end{bmatrix} \tag{B.2}$$

When $i+1>n$, it is replaced by 1.

$T_{(i+1)i}$ transforms the expression in the $(i+1)$-th coordinate system to the ith coordinate system. The inverse transformation matrix $T_{i(i+1)}$ has the following property.

$$T_{i(i+1)} = \begin{bmatrix} \cos\theta_i & \sin\theta_i & 0 & -a_{i(i+1)} \\ -\cos\alpha_{i(i+1)}\sin\theta_i & \cos\alpha_{i(i+1)}\sin\theta_i & \sin\alpha_{i(i+1)} & -R_i\sin\alpha_{i(i+1)} \\ \sin\alpha_{i(i+1)}\sin\theta_i & -\sin\alpha_{i(i+1)}\sin\theta_i & \cos\alpha_{i(i+1)} & -R_i\cos\alpha_{i(i+1)} \\ 0 & 0 & 0 & 1 \end{bmatrix} \tag{B.3}$$

For origami of zero-thickness sheets, the offsets and link lengths of each vertex are zero. For the origami of thick panels, these parameters need to be revised due to fold displacement. The kinematic behaviours of thick-panel origami discussed in this work will be based on the solutions of Eq. (B.1).

The focus of this research is on the thick-panel origami consisting of six panels, which are further modelled as a 6R linkage. Thus, Eq. (B.1) can be simplified as

$$E = T_{21}T_{32}T_{43} - T_{61}T_{56}T_{45} = 0_{4\times4} \tag{B.4}$$

where $0_{4\times4}$ is a null matrix.

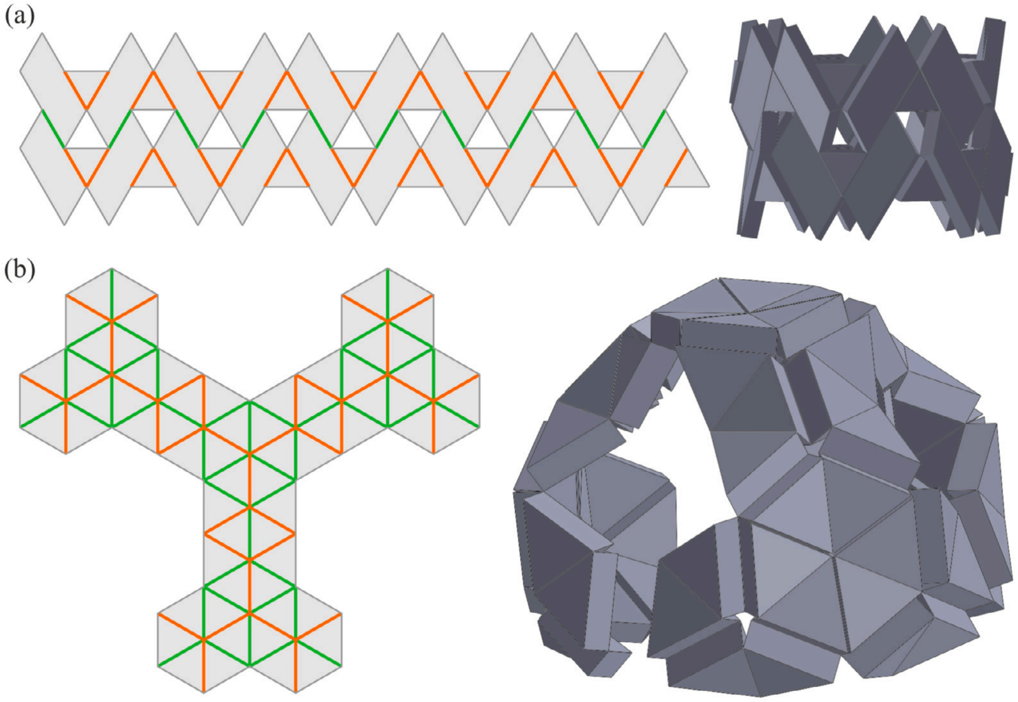

Fig. 26. Other configurations based on **(a)** Unit m_2 and **(c)** a combination of Units a_1 and b_1.

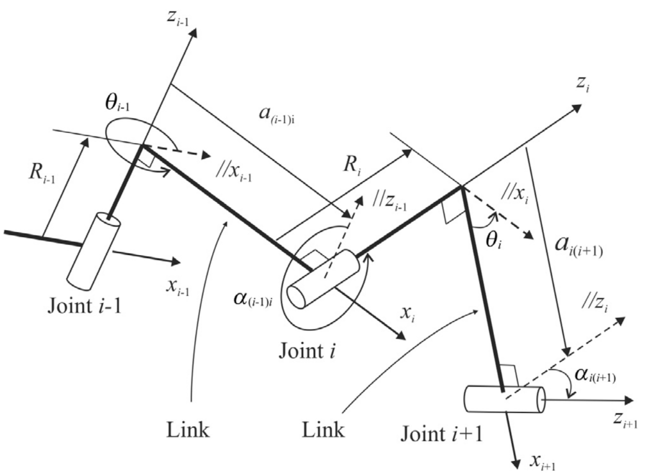

Fig. B.27. DH notations of adjacent links connected by revolute joints.

Appendix C. 6R spatial overconstrained linkages

There are a limited number of spatial linkages that are overconstrained, as summarised by You and Chen [28]. Hence, it is feasible to exhaustively map all the linkages with thick-panel origami. One 4R linkage, i.e., the Bennett linkage, has been well studied [17,40]. The two 5R linkages, i.e., the Myard linkage [41] and Goldberg 5R linkage [42], have less symmetry and are not desirable for tessellations. Thus, the research only focuses on 6R linkages. According to their geometric conditions, these linkages are categorised into three groups shown in Table C.6, Table C.7, and Table C.8.

The first group, Table C.6, includes the linkages whose joint offsets have to be all zero. The second group, Table C.7, and the third group, Table C.8, are the linkages derived from the Bennet linkage and the Bricard linkage, respectively. These cases also permit non-zero joint offsets. Whilst some linkages are not included, such as the plano-spherical hybrid linkage [43] as well as the Yu and Baker's syncopated linkage [44], they can be regarded as special cases or derivatives of the ones summarised here. The three tables are the foundation for creating a mapping between overconstrained linkages and thick-panel origami.

Appendix D. Additional morphing units

This appendix summarises units that do not satisfy the selection criteria detailed in Section 2.

D.1. Multi-DoF units

Fig. D.28(a) is a unit based on the Waldron hybrid linkage, where $\alpha_{\mathrm{P1}} = \alpha_{\mathrm{P22}} = \alpha_{\mathrm{P23}} = \alpha_{\mathrm{P3}}$ and $\alpha_{\mathrm{P4}} = \alpha_{\mathrm{P55}} = \alpha_{\mathrm{P56}} = \alpha_{\mathrm{P6}}$. The case was also reported by [60]. Fig. D.28(b) is a special case Unit c_2 derived from the line-symmetric Bricard linkage, where $\alpha_{\mathrm{P1}} = \alpha_{\mathrm{P22}} = \alpha_{\mathrm{P4}} = \alpha_{\mathrm{P55}}$ and $\alpha_{\mathrm{P23}} = \alpha_{\mathrm{P3}} = \alpha_{\mathrm{P56}} = \alpha_{\mathrm{P6}}$. Both units have two DoFs at the flat state due to the aligned folds, i.e., folds 2 and 6 as well as folds 3 and 5. When these folds are fully folded, each unit can move into a single-DoF path via the newly aligned folds 1 and 4.

D.2. Units with physical interference

Figs. D.28(c) - D.28(g) illustrate single-DoF units with physical collisions. These units are based on the Bennett 6R hybrid linkage, the Bricard linkage, and the Sarrus linkage and should satisfy the relevant geometric conditions. For instance, the unit in Fig. D.28(e) is derived from the plane-symmetric Bricard linkage. Hence, $\alpha_{\mathrm{P1}} = \alpha_{\mathrm{P6}}$, $\alpha_{\mathrm{P22}} = \alpha_{\mathrm{P56}}$, $\alpha_{\mathrm{P23}} = \alpha_{\mathrm{P55}}$, and $\alpha_{\mathrm{P3}} = \alpha_{\mathrm{P4}}$. The overlapping areas of these units are marked in red. Currently, self-intersection of these structures is analysed through SOLIDWORKS simulations. However, a geometric model could be developed in the future to predict which structures may cause physical interference.

Appendix E. Demonstration process

The design methodology specified in Section 2 not only yields a series of morphing units, but also concludes which linkages or which

Table C.6
Geometric conditions of 6R overconstrained linkages whose joint offsets are all zero.

Linkage	Link length	Link twist	Other conditions
Extended Myard 6R linkage [41]	$a_{12} = a_{34} = a_{45} = a_{61}$ $a_{23} = a_{56} = 0$	$\alpha_{12} = \alpha_{34} = \alpha_{45} = \alpha_{61}$ $\alpha_{23} + \alpha_{56} = 360°$	
Goldberg 6R linkage (series) [42]	$a_{12} = a_{34}$ $a_{23} = a_{45} + a_{45} + a_{61}$	$\alpha_{12} = \alpha_{34}$ $\alpha_{23} = \alpha_{45} + \alpha_{45} + \alpha_{61}$	$\frac{\sin \alpha_{i(i+1)}}{a_{i(i+1)}} = k_B \ (i = 1,4,5,6)$
Goldberg 6R linkage (L-shaped) [42]	$a_{12} = a_{34} + a_{56}$ $a_{23} = a_{45} + a_{61}$	$\alpha_{12} = \alpha_{34} + \alpha_{56}$ $\alpha_{23} = \alpha_{45} + \alpha_{61}$	$\frac{\sin \alpha_{i(i+1)}}{a_{i(i+1)}} = k_B \ (i = 3,4,5,6)$
Wohlhart double-Goldberg linkage [45]	$a_{12} = a_{34}$ $a_{23} = a_{56} = b + c$ $a_{45} = a_{61}$	$\alpha_{12} = \alpha_{34}$ $\alpha_{23} = \alpha_{56} = \beta + \gamma$ $\alpha_{45} = \alpha_{61}$	$\frac{\sin \alpha_{i(i+1)}}{a_{i(i+1)}} = k_B \ (i = 1,4)$ $\frac{\sin \beta}{b} = \frac{\sin \gamma}{c} = k_B$
Chen & You double-Goldberg linkage 1 [46]	$a_{12} = a_{45}$ $a_{23} = a_{56} = b - c$ $a_{34} = a_{61}$	$\alpha_{12} = \alpha_{45}$ $\alpha_{23} = \alpha_{56} = \beta - \gamma$ $\alpha_{34} = \alpha_{61}$	$\frac{\sin \alpha_{i(i+1)}}{a_{i(i+1)}} = k_B \ (i = 1,4)$ $\frac{\sin \beta}{b} = \frac{\sin \gamma}{c} = k_B$ $\tan \frac{\alpha_{12}}{2} \tan \frac{\alpha_{61}}{2} = \tan \frac{\beta}{2} \tan \frac{\gamma}{2}$
Chen & You double-Goldberg linkage 2 [46]	$a_{12} = a_{34}$ $a_{23} = a_{56} = b - c$ $a_{45} = a_{61}$	$\alpha_{12} = \alpha_{34}$ $\alpha_{23} = \alpha_{56} = \beta - \gamma$ $\alpha_{45} = \alpha_{61}$	Same as Chen & You double-Goldberg linkage 1
Altmann linkage [47] [48]	$a_{12} = a_{45}$, $a_{34} = a_{61}$ $a_{23} = a_{56} = 0$	$\alpha_{12} = \alpha_{23} = 90°$ $\alpha_{45} = \alpha_{56} = 90°$ $\alpha_{34} = \alpha_{61} = 270°$	

Table C.7
Geometric conditions of 6R overconstrained linkages derived from Bennett linkage with non-zero offsets.

Linkage	Link length	Link twist	Joint offset
Dietmaier 6R linkage [49]	$a_{23} = a_{56}$	$\alpha_{23} = \alpha_{56}$ $\frac{\sin \alpha_{12}}{a_{12}} = \frac{\sin \alpha_{61}}{a_{61}}, \quad \frac{\sin \alpha_{34}}{a_{34}} = \frac{\sin \alpha_{45}}{a_{45}}$ $\frac{\sin \alpha_{12}}{a_{12}} (\cos \alpha_{12} + \cos \alpha_{61})$ $= \frac{\sin \alpha_{34}}{a_{34}} (\cos \alpha_{34} + \cos \alpha_{45})$	$R_3 = R_6 = 0$ $R_1 = R_5$ $R_2 = R_4$
Bennett-joint 6R linkage [50]	$a_{12} = a_{34}$ $a_{23} = a_{56}$ $a_{45} = a_{61}$	$\alpha_{12} = \alpha_{34}$ $\alpha_{23} = \alpha_{56}$ $\alpha_{34} = \alpha_{61}$ $\frac{\sin \alpha_{12}}{a_{12}} = \frac{\sin \alpha_{45}}{a_{45}}$	$R_1 = R_4 = 0$ $R_2 = R_5 \ (R_6)$ $R_3 = R_6 \ (R_5)$
Bennett 6R hybrid linkage [51]	$a_{12} = a_{34} = 0$ $a_{45} = a_{61} = 0$		$R_1 = R_4 = 0$
Double-Hooke's-joint linkage [52]	$a_{12} = a_{34} = 0$ $a_{45} = a_{61} = 0$	$\alpha_{12} = \alpha_{34} = \alpha_{45} = \alpha_{61} = 90°$	$R_i = 0 \ (i = 1, \dots, 4)$
Sarrus linkage [51,53]	$a_{12} = a_{34}$ $a_{45} = a_{61}$ $a_{23} = a_{56} = 0$	$\alpha_{12} = \alpha_{34} = \alpha_{45} = \alpha_{61} = 0$ $\alpha_{23} = \alpha_{56} \neq 180°$	
Waldron hybrid linkage [54]		$\alpha_{23} + \alpha_{61} = 180° + \alpha_{45}$ $\alpha_{34} + \alpha_{56} = 180° = +\alpha_{12}$ $\frac{a_{12}}{a_{61}} = -\frac{\sin \alpha_{12}}{\sin \alpha_{61}}, \quad \frac{a_{34}}{a_{45}} = -\frac{\sin \alpha_{34}}{\sin \alpha_{45}}$	$R_1 = R_4 = 0$ $\frac{R_2}{R_3} = \frac{\sin \alpha_{45}}{\sin \alpha_{61}}$ $\frac{R_5}{R_6} = \frac{\sin \alpha_{12}}{\sin \alpha_{34}}$

bases cannot be transformed into a mobile unit with uniform thickness. This appendix illustrates the evaluation steps on selected linkages and bases. Some immobile cases are found and the evaluation process is transferable to other overconstrained linkages and origami bases.

E.1. Extended myard 6R linkage

According to Table C.6, the extended Myard 6R linkage requires all joint offsets to be zero. It is hence examined on all bases in Fig. 1 as follows.

- If the linkage is transformed to an SVP and can still be mobile, the fold arrangement has to be either of the two cases shown in Fig. E.29(a). This is because the linkage requires $a_{23} = a_{56} = 0$ and $\alpha_{23} + \alpha_{56} = 360°$.
  - Case 1 would not work as the link length condition $a_{12} = a_{34} = a_{45} = a_{51}$ cannot be satisfied, no matter how folds 1 and 4 are arranged.
  - Case 2 has two sub-cases satisfying the link length requirement, as shown in Fig. E.29(b).

Table C.8
Geometric conditions of 6R overconstrained linkages derived from Bricard linkage with non-zero offsets.

Linkage	Link length	Link twist	Joint offset
Line-symmetric Bricard linkage [23,55][56]	$a_{12} = a_{45}$ $a_{23} = a_{56}$ $a_{34} = a_{61}$	$\alpha_{12} = \alpha_{45}$ $\alpha_{23} = \alpha_{56}$ $\alpha_{34} = \alpha_{61}$	$R_1 = R_4$ $R_2 = R_5$ $R_3 = R_6$
Plane-symmetric Bricard linkage [23,55][56]	$a_{12} = a_{61}$ $a_{23} = a_{56}$ $a_{34} = a_{45}$	$\alpha_{12} + \alpha_{61} = 360°$ $\alpha_{23} + \alpha_{56} = 360°$ $\alpha_{34} + \alpha_{45} = 360°$	$R_1 = R_4 = 0$ $R_2 = R_6$ $R_3 = R_5$
Schatz linkage [57,58]	$a_{12} = a_{56}$ $a_{23} = a_{34} = a_{45}$ $a_{61} = \sqrt{3}a_{23}$	$\alpha_{12} = \alpha_{23} = \alpha_{34} = 90°$ $\alpha_{45} = \alpha_{56} = 90°$ $\alpha_{61} = 0$	$R_1 = -R_6$ $R_2 = R_3 = R_4 = R_5 = 0$
Wohlhart 6R linkage [59]	$a_{12} = a_{23}$ $a_{34} = a_{45}$ $a_{56} = a_{61}$	$\alpha_{12} + \alpha_{23} = 360°$ $\alpha_{34} + \alpha_{45} = 360°$ $\alpha_{56} + \alpha_{61} = 360°$	$R_1 = R_3 = R_5 = 0$ $R_2 + R_4 + R_6 = 0$

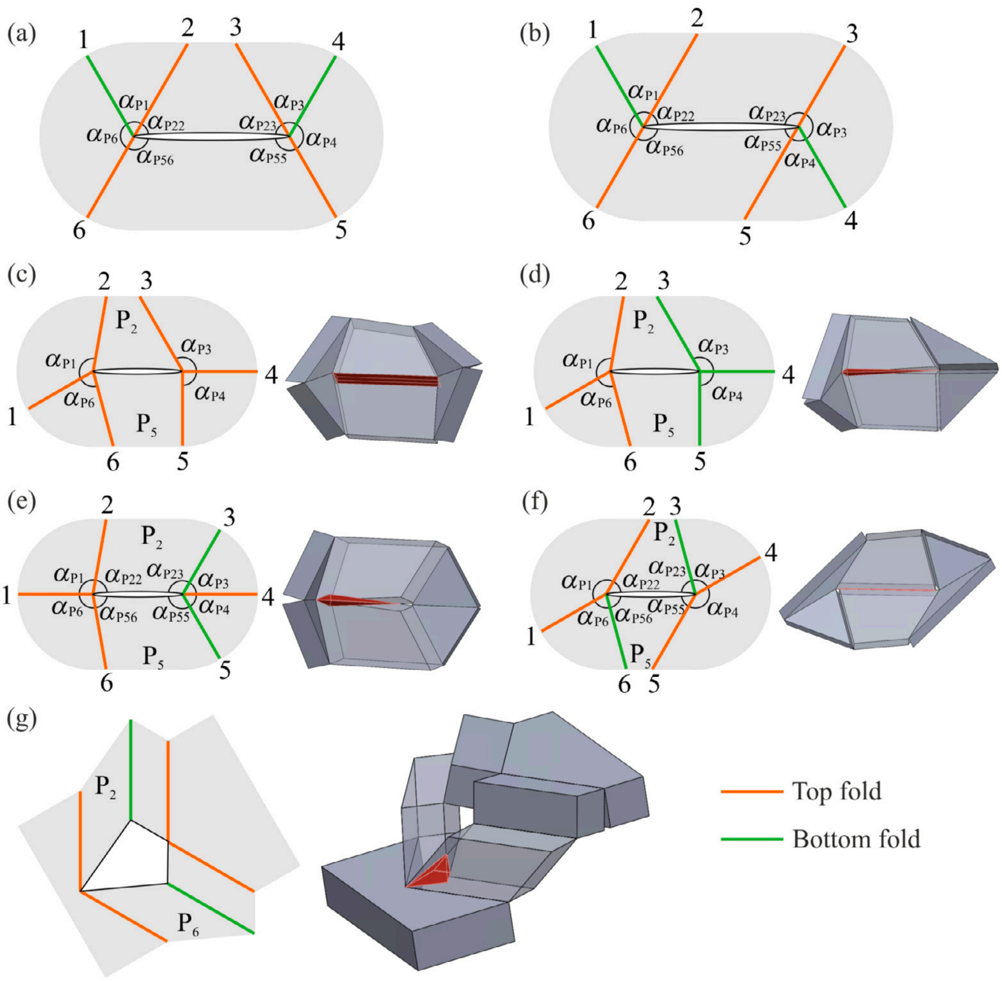

Fig. D.28. Morphing units with more than one DoF or physical collisions. **(a)** Unit based on the Waldron hybrid linkage. **(b)** Unit based on the line-symmetric Bricard linkage. Both start with two DoFs and then reduce to a single mobility. **(c)** and **(d)** Units based on Bennett 6R hybrid linkage. **(e)** and **(f)** Units based on the plane-symmetric and line-symmetric Bricard linkages, respectively. The collision occurs between P_2 and P_5 on these four units. **(e)** Unit based on the Sarrus linkage and the interference exists between P_2 and P_6. The interfered area of each unit is identified by the SOLIDWORKS simulation and marked in red.

  - Case 2.1 gives $\alpha_{12} = 360° - \alpha_{P1}$ and $\alpha_{34} = \alpha_{P3}$. If they satisfy the link twist condition $\alpha_{12} = \alpha_{34}$, we can get $\alpha_{P1} + \alpha_{P3} = 360°$, conflicting the constraints in Eq. (2) and Table 1.
  - Case 2.2 meets the link twist condition with all folds on the same surface. The unit thus becomes a 6R spherical linkage and the only valid motions are caused by aligned folds.
- If the unit is not based on the SVP, only the patterns in Figs. E.29(c) and E.29(d) have zero offsets. However, the link twist conditions are unsatisfied.

Given the analysis above, it is concluded that the extended Myard 6R linkage cannot be used to design morphing units from any base in Fig. 1.

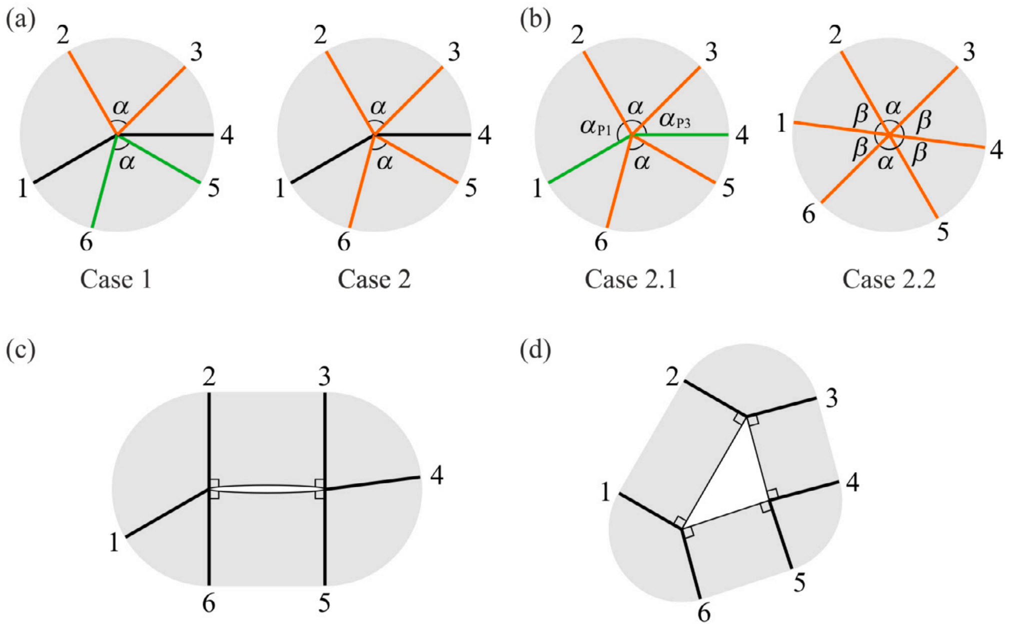

Fig. E.29. Evaluation of the extended Myard 6R linkage on a morphing unit. **(a)** and **(b)** Possible cases to meet certain geometric conditions on the SVP. **(c)** and **(d)** Possible cases to meet the zero joint offsets on the SSP and TVP.

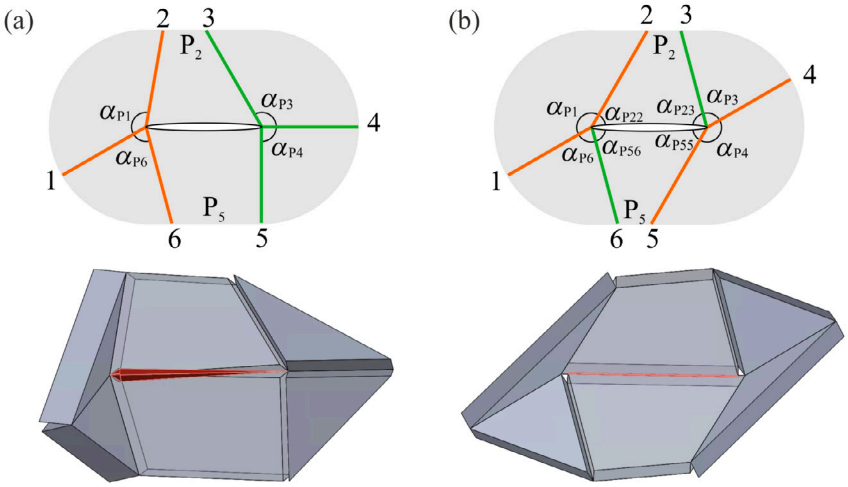

Fig. E.30. Patterns that satisfy **(a)** the Bennett 6R hybrid linkage and **(b)** the line-symmetric Bricard linkage. The physical interference exists between P_2 and P_5.

E.2. Altmann linkage and Schatz linkage

The second example looks at the Altmann linkage and the Schatz linkage on the SVP. The former linkage requires $\alpha_{12} = \alpha_{23} = \alpha_{45} = \alpha_{56} = 90°$, which yields $\alpha_{P1} + \alpha_{P2} + \alpha_{P4} + \alpha_{P5} \geq 360°$ according to Eq. (3). The result conflicts with constraints in Eq. (2) and Table 1. Similarly, the Schatz linkage requires $\alpha_{12} = \alpha_{23} = \alpha_{34} = \alpha_{45} = \alpha_{56} = 90°$, leading to the same geometric conflict.

E.3. Bennett 6R hybrid linkage

The Bennett 6R hybrid linkage is evaluated on the SSP. The pattern in Fig. E.30(a) satisfies the linkage condition and it has a single mobility. Only when $\alpha_{P1} + \alpha_{P6} > 180°$ and $\alpha_{P3} + \alpha_{P4} > 180°$, the dihedral angle range in Eq. (1) could be satisfied. However, the corresponding 3D model simulated in SOLIDWORKS indicates that the lower edge of P_2 interferes with the upper edge of P_5 when the unit is folded from flat. The overlapping areas are highlighted in red as shown in Fig. E.30(a). Due to the physical interference, such cases are not counted as mobile units.

The physical collision may also occur to linkages that are already feasible to design morphing units. Notably, Unit c_2 discussed before is based on the line-symmetric Bricard linkage. It could have an alternative fold arrangement as shown in Fig. E.30(b), where $\alpha_{P1} = \alpha_{P4}$, $\alpha_{P22} = \alpha_{P55}$, $\alpha_{P23} = \alpha_{P56}$, and $\alpha_{P3} = \alpha_{P6}$. If the dihedral angle range in Eq. (1) is met, the sum of α_{P1} and α_{P22} should exceed 180°. Nonetheless, a collision between adjacent panels is detected, as shown in Fig. E.30(b). Hence, the case is considered immobile unless the overlapping parts are removed.

E.4. Wohlhart 6R linkage

The Wohlhart 6R linkage has found a mobile counterpart on the SSP as Unit m_1. When it comes to the TVP, the situation turns out to be different.

The linkage requires joint offsets R_1, R_3, and R_5 to be all zero as detailed in Table C.8, which is normally not the case of a TVP. To create zero joint offsets on non-single-vertex 2D patterns, a few strategies have been introduced in Fig. 4. Although the pattern in Fig. 4(a) naturally meets the requirement of R_1, R_3, and R_5, another geometric condition of the linkage $R_2 + R_4 + R_6 = 0$ cannot be satisfied. This is because the offsets of other folds become $R_2 = a$, $R_4 = b$, and $R_6 = c$, where a, b, and c are the side lengths of the triangular void. As for the parallel folds in 4(c), at least three zero link twists will be produced to ensure R_1, R_3, and R_5 are zero, making it impossible to meet the linkage's link twist condition such as $\alpha_{12} + \alpha_{23} = 360°$.

Data availability

No data was used for the research described in the article.

References

[1] Sarraf N, Rodriguez KR, Qian L. Modular reconfiguration of DNA origami assemblies using tile displacement. Sci Robot 2023;8(77):eadf1511.
[2] Kuribayashi K, Tsuchiya K, You Z, Tomus D, Umemoto M, Ito T, et al. Self-deployable origami stent grafts as a biomedical application of Ni-rich TiNi shape memory alloy foil. Mater Sci Engineering: A 2006;419(1–2):131–7.
[3] Thrall AP, Quaglia C. Accordion shelters: A historical review of origami-like deployable shelters developed by the US military. Eng Struct 2014;59:686–92.
[4] Georgakopoulos SV, Zekios CL, Sattar-Kaddour A, Hamza M, Biswas A, Clark B, et al. Origami antennas. IEEE Open J Antennas Propag 2021;2:1020–43.
[5] Rus D, Tolley MT. Design, fabrication and control of origami robots. Nat Rev Mater 2018;3(6):101–12.
[6] Zhang Z, Tang S, Fan W, Xun Y, Wang H, Chen G. Design and analysis of hybrid-driven origami continuum robots with extensible and stiffness-tunable sections. Mech Mach Theory 2022;169:104607.
[7] Lee D-Y, Kim S-R, Kim J-S, Park J-J, Cho K-J. Origami wheel transformer: A variable-diameter wheel drive robot using an origami structure. Soft Robot 2017;4(2):163–80.
[8] Wu S, Ze Q, Dai J, Udipi N, Paulino GH, Zhao R. Stretchable origami robotic arm with omnidirectional bending and twisting. Proc Natl Acad Sci 2021;118(36):e2110023118.
[9] Li S, Stampfli JJ, Xu HJ, Malkin E, Diaz EV, Rus D, et al. A vacuum-driven origami "magic-ball" soft gripper. In: 2019 international conference on robotics and automation. IEEE; 2019, p. 7401–8.
[10] Miyashita S, Guitron S, Ludersdorfer M, Sung CR, Rus D. An untethered miniature origami robot that self-folds, walks, swims, and degrades. In: 2015 IEEE international conference on robotics and automation. IEEE; 2015, p. 1490–6.
[11] Rus D, Sung C. Spotlight on origami robots. Sci Robot 2018;3(15):eaat0938.
[12] Jeong D, Lee K. Design and analysis of an origami-based three-finger manipulator. Robotica 2018;36(2):261–74.
[13] Onal CD, Wood RJ, Rus D. An origami-inspired approach to worm robots. IEEE/ASME Trans Mechatronics 2012;18(2):430–8.
[14] Kan Z, Zhang Y, Yang Y, Tse YA, Wang MY. An origami-inspired monolithic soft gripper based on geometric design method. In: 2019 2nd IEEE international conference on soft robotics. IEEE; 2019, p. 470–6.
[15] Kresling B. The fifth fold: complex symmetries in Kresling-origami patterns. Symmetry Cult Sci 2020;31:403–16.
[16] Chen Y, Peng R, You Z. Origami of thick panels. Science 2015;349(6246):396–400.
[17] Zhang X, Chen Y. Mobile assemblies of Bennett linkages from four-crease origami patterns. Proc R Soc A: Math Phys Eng Sci 2018a;474(2210):20170621.
[18] Zhang X, Chen Y. The diamond thick-panel origami and the corresponding mobile assemblies of plane-symmetric Bricard linkages. Mech Mach Theory 2018b;130:585–604.
[19] Pratapa PP, Bellamkonda A. Thick panel origami for load-bearing deployable structures. Mech Res Commun 2022;124:103937.
[20] Chen Y, Feng H, Ma J, Peng R, You Z. Symmetric waterbomb origami. Proc R Soc A: Math Phys Eng Sci 2016;472(2190):20150846.
[21] Yang F, Zhang M, Ma J, You Z, Yu Y, Chen Y, et al. Design of single degree-of-freedom triangular resch patterns with thick-panel origami. Mech Mach Theory 2022a;169:104650.
[22] Bennett GT. A new mechanism. Engineering 1903;76:777.
[23] Bricard R. Leçons de cinématique, vol. 1, Gauthier-Villars; 1926.
[24] Wang C, Zhang D, Li J, You Z. Kirigami-inspired thick-panel deployable structures. Int J Solids Struct 2022;251:111752.
[25] Yang J, Zhang X, Chen Y, You Z. Folding arrays of uniform-thickness panels to compact bundles with a single degree of freedom. Proc R Soc A 2022b;478(2261):20220043.
[26] Yang J, You Z. Cutting and folding thick-panel miura-ori with one DoF. In: International design engineering technical conferences and computers and information in engineering conference, vol. 87363. American Society of Mechanical Engineers; 2023, V008T08A044.
[27] Li J, Zhang X, An S, Zhu Z, Deng Z, You Z. Kirigami-inspired foldable 3D cellular structures with a single degree of freedom. Int J Solids Struct 2022;244:111587.
[28] You Z, Chen Y. Motion structures: deployable structural assemblies of mechanisms. Taylor & Francis; 2012.
[29] Feng H, Chen Y, Dai JS, Gogu G. Kinematic study of the general plane-symmetric Bricard linkage and its bifurcation variations. Mech Mach Theory 2017;116:89–104.
[30] Song C, Chen Y, Chen I-M. A 6R linkage reconfigurable between the line-symmetric Bricard linkage and the Bennett linkage. Mech Mach Theory 2013;70:278–92.
[31] Verrill H. Origami tessellations. In: Bridges: mathematical connections in art, music, and science. 1998, p. 55–68.
[32] Liu C, Maiolino P, You Z. A 3d-printable robotic gripper based on thick panel origami. Front Robot AI 2021;8:730227.
[33] Liu C, He L, Wang S, Williams A, You Z, Maiolino P. Exploring kinematic bifurcations and hinge compliance for in-hand manipulation: How could thick-panel Origami contribute? Adv Intell Syst 2024;2300691.
[34] Liu C, Maiolino P, Yang Y, You Z. Hybrid soft-rigid deployable structure inspired by thick-panel origami. In: International design engineering technical conferences and computers and information in engineering conference, vol. 83990. American Society of Mechanical Engineers; 2020, V010T10A080.
[35] Liu C, You Z, Maiolino P. Kinematics of an origami inspired millipede robot. In: International design engineering technical conferences and computers and information in engineering conference, vol. 86281. American Society of Mechanical Engineers; 2022, V007T07A062.
[36] Liu C. Origami-inspired kinematic morphing surfaces [Ph.D. thesis], University of Oxford; 2023.
[37] Wang C, Li J, Zhang D. Motion singularity analysis of the thick-panel kirigami. Mech Mach Theory 2023;180:105162.
[38] Yang Y. Modular origami-inspired kinematic metamaterials [Ph.D. thesis], University of Oxford; 2020.
[39] Denavit J, Hartenberg RS. A kinematic notation for lower-pair mechanisms based on matrices. American Society of Mechanical Engineers; 1955.
[40] Zhang X, Chen W. Folding a flat rectangular plate of uniform-thickness panels using miura-ori. Int J Mech Sci 2023;108570.
[41] Chen Y, You Z. An extended myard linkage and its derived 6R linkage. J Mech Des 2008;130:052301.
[42] Goldberg M. New five-bar and six-bar linkages in three dimensions. Trans Am Soc Mech Eng 1943;65(6):649–56.
[43] Zhang K, Dai JS. Screw-system-variation enabled reconfiguration of the Bennett plano-spherical hybrid linkage and its evolved parallel mechanism. J Mech Des 2015;137(6):062303.
[44] Hon-Cheung Y, Baker JE. On the generation of new linkages from Bennett loops. Mech Mach Theory 1981;16(5):473–85.
[45] Wohlhart K. Merging two general goldberg 5R linkages to obtain a new 6R space mechanism. Mech Mach Theory 1991;26(7):659–68.
[46] Chen Y, You Z. Spatial 6R linkages based on the combination of two Goldberg 5R linkages. Mech Mach Theory 2007;42(11):1484–98.
[47] Grodzinski P, M'Ewen E. Link mechanisms in modern kinematics. Proc Inst Mech Eng 1954;168(1):877–96.
[48] Baker JE. A geometrico-algebraic exploration of Altmann's linkage. Mech Mach Theory 1993;28(2):249–60.
[49] Dietmaier P. A new 6R space mechanism. In: Proceeding 9th world congress IFToMM, vol. 1. 1995, p. 52–6.
[50] Mavroidis C, Roth B. Analysis and synthesis of overconstrained mechanism. In: International design engineering technical conferences and computers and information in engineering conference, vol. 12846. American Society of Mechanical Engineers; 1994, p. 115–33.
[51] Bennett GT. LxxVII. The parallel motion of Sarrut and some allied mechanisms. Lond Edinb Dublin Philos Mag J Sci 1905;9(54):803–10.
[52] Baker JE. Displacement–closure equations of the unspecialised double-Hooke's-joint linkage. Mech Mach Theory 2002;37(10):1127–44.
[53] Sarrus P. Note sur la transformation des mouvements rectilignes alternatifs, en mouvements circulaires, et reciproquement. Comptes Rendus, Acad Sci Paris 1853;36:1036–8.
[54] Waldron KJ. Hybrid overconstrained linkages. J Mech 1968;3(2):73–8.
[55] Baker JE. An analysis of the Bricard linkages. Mech Mach Theory 1980;15(4):267–86.
[56] Mavroidis C, Roth B. New and revised overconstrained mechanisms. J Mech Des 1995;117(1):75–82.
[57] Phillips J. Freedom in machinery: Introducing screw theory, vol. 1, Cambridge University Press; 1984.
[58] Lee C, Dai J. Configuration analysis of the Schatz linkage. Proc Inst Mech Eng Part C: J Mech Eng Sci 2003;217(7):779–86.
[59] Wohlhart K. A new 6R space mechanism. In: Proceedings of the seventh world congress on the theory of machines and mechanisms, vol. 1. 1987, p. 193–8.
[60] Wang C, Li J, You Z. A kirigami-inspired foldable model for thick panels. In: The 7th international meeting on origami in science, mathematics and education. 2018b, p. 5–7.